PHYSICAL REVIEW B VOLUME 25, NUMBER 4 15 FEBRUARY 1982

Helium diffraction from the GaAs(110) surface and the generation of helium-surface potentials

R. B. Laughlin
Bell Laboratories, Murray Hill, New Jersey 07974
(Received 28 May 1981)

A theoretical analysis of the helium diffraction experiments performed on the GaAs(110) surface by Cardillo, Becker, Sibener, and Miller is presented. Dynamic scattering calculations for several model potentials approximating that of the surface are presented. These suggest that the surface is a smoothly corrugated soft wall with a peak-to-trough distance along the [001] direction of ~ 1 Å and an attractive well depth of ~ 7 meV. Existing methods for generating van der Waals potentials are reviewed and an explanation is suggested for their poor performance in the case of helium. New semiempirical rules fit to the known helium rare-gas potentials and consistent with the recent results of Esjberg and Nørskov are proposed. These are used to construct an approximate potential for GaAs(110), which we show to agree qualitatively with the empirically fit potential. The classical turning-point surface of this potential lies 3.5 Å above the As nucleus. Scattering calculations performed on this potential are shown to agree poorly with experiment. We conclude from this that the scattering is very sensitive to nuances in the potential, and that very accurate surface charge densities will be required before a potential capable of scattering in agreement with experiment can be constructed.

I. INTRODUCTION

The diffraction of helium atoms from surfaces is a powerful new tool for surface structure analysis still in its infancy.[1,2] At present, its usefulness as a diagnostic tool is impaired by the difficulty of interpreting data from highly corrugated surfaces,[3] notably the semiconductors.[4,5] From a theoretical standpoint, the most significant source of this difficulty has been the absence of rules for generating the scattering potential given the positions of the target nuclei. In this paper, we attempt to shed some light on this problem by discussing in detail the diffraction of helium from the GaAs(110) surface.

The situation in the theory of atom diffraction from surfaces is well illustrated by the case of LiF. Like graphite,[6] LiF has been studied extensively both experimentally[7] and theoretically.[8] Nevertheless, scattering calculations based on "realistic" potentials capable of producing good agreement with experiment have never been performed (although Wolken[9] has performed dynamic scattering calculations for an approximate model potential). Garcia[8] has obtained excellent agreement with the diffraction intensities from LiF(100) observed by Boato *et al.*,[7] by modeling the surface as an infinitely hard wall. The maximum peak-to-trough distance of this wall, 0.3 Å in each principal direction, is sufficiently small[7,8,10] that the depth of the van der Waals attractive well bounding the wall can be inferred from kinematic analysis[7] of the selective-adsorption resonance positions. This depth (~ 8 meV) is found[7,8] to be small compared with the kinetic energy (~ 21 meV) of the probe. While the complete scattering potential for LiF(100) is not known, some information about it has been obtained[11] from selective-adsorption line shapes and anticrossing splittings. The latter analysis has been performed sufficiently thoroughly by Carlos and Cole[12] for graphite that the helium-graphite potential can be said to be known accurately, up to arbitrariness in the location of the origin. This is not true for any other surface.

Attempts to calculate scattering potentials from first principles have been discouraging. Freeman[13] has calculated the helium-graphite potential using the Gordon-Kim[14] technique to obtain an attractive-well depth roughly $\frac{1}{3}$ (Ref. 13) of the measured[6] value and hard-wall parameters agreeing poorly with the data.[6] Somewhat better results have been obtained by Tsuchida,[15] who has represented LiF as a sum of known He-Ne and He-He potentials and obtained attractive well depth and corrugation parameters agreeing to within 30% of experiment. Except for the work of

Tsuchida[15] and that of Esjberg and Nørskov[16] on the Al(110) surface, there has been no success at predicting corrugation parameters. A strong correlation between the attractive depth and the polarization properties of the target is known[1] to exist.

In this paper, we approach the problem of helium-surface potentials both using GaAs(110) as a prototype surface on which to test both potential generation and diffraction from those potentials. There are two reasons why GaAs(110) is superior to either LiF(100) or graphite in this regard: (1) Its structure is well known,[17] so that information contained in the scattering signal tells us about the potential rather than the structure. (2) It is nontrivial topographically, and thus its diffraction intensities are difficult to fit. This topography is illustrated in Fig. 1. GaAs(110) is composed of zig-zag chains of Ga and As atoms arranged in parallel rows on the surface. The separation between the chains is 5.59 Å, the repeat distance along the chain is 3.95 Å, and the vertical drop between surface chains and the floor of the trough separating them is 1.98 Å, before reconstruction. As the Ga dangling bond contains no electrons, the system reconstructs[17] by tipping the chains 27°. This raises the As atom 0.46 Å, lowers the Ga atom 0.19 Å, and increases the drop between the As atom in the surface and those in the second layer to 2.44 Å. As we shall show in Sec. III, this surface has three times the corrugation of LiF in one direction.

The plan of the paper is as follows. In Sec. II, we briefly review the principles of scattering from hard walls and show how these bear on scattering from the more realistic potentials suitable for describing GaAs(110). In Sec. III, we review the GaAs(110) helium-scattering data of Cardillo *et al.*,[5] and analyze these using the empirical-model potentials. In Sec. IV, we discuss the problem of generating a scattering potential, and propose ways of circumventing the difficulties commonly encountered when trying to do so. In Sec. V, we discuss the application of the rules for generating potentials discussed in Sec. IV to GaAs(110). In Sec. VI, we summarize our results.

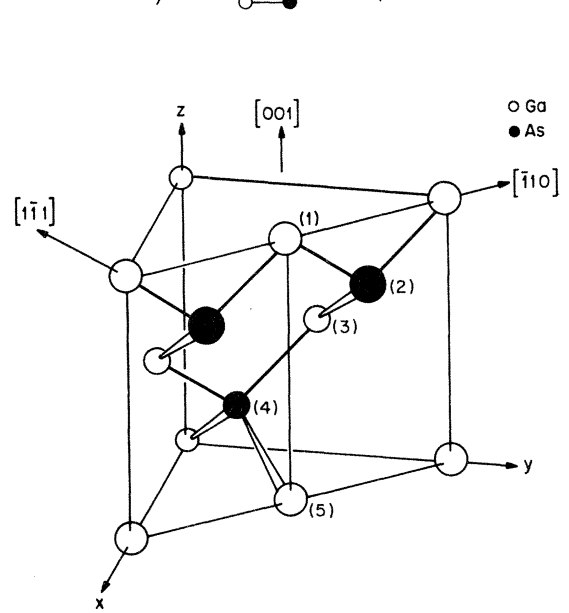

FIG. 1. Schematic drawing of GaAs(110) structure. Atoms (1) and (2) belong to one surface chain. Atom (5) is the analog of atom (1) on an adjacent chain. Atoms (3) and (4) form the floor of the trough separating the two chains.

II. ELASTIC SCATTERING FROM SOFT WALLS

Following Garibaldi *et al.*[18] and Garcia *et al.*[19] we consider a one-dimensional wall, the height of which above the surface at x is $h(x)$. We let the probe atoms impinge on the surface with polar angle θ and momentum q_0, and write[20] for the wave function

$$\psi = e^{ikx}\exp[i(q_0^2-k^2)^{1/2}z] + \sum_G a_G e^{i(k+G)x} \times \exp\{-i[q^2-(k+G)^2]^{1/2}z\}, \quad (1)$$

where $k=q_0\sin(\theta)$ is the component of momentum in the plane of the surface, and each G is a reciprocal-lattice vector. The scattering amplitudes, a_G, related to the probabilities I_G for adding transverse momentum G to the probe by

$$I_G = \frac{\cos(\theta')}{\cos(\theta)} |a_G|^2, \quad (2)$$

where θ and θ' are the angles of incidence and exit, must be picked to make the wave function zero at the surface, in the manner

$$0=1+\sum_G a_G e^{iGx}\exp(-i\{(q_0^2-k^2)^{1/2}+[q_0^2-(k+G)^2]^{1/2}\}h(x)) . \quad (3)$$

This is possible, in general, only when the surface is trivial, since the Rayleigh approximation[20] [Eq. (1)] forces the expansion set to be incomplete. However, if the surface is weakly corrugated [$|\partial h/\partial x| \lesssim 0.1$ (Ref. 18)] one can make the further approximation[18] that the normal momentum transfer is independent of G,

$$(q_0^2-k^2)^{1/2}+[q_0^2-(k+G)^2]^{1/2}\simeq q , \quad (4)$$

in which case the scattering complitudes can be written as a definite integral of the form[18]

$$a_G\simeq\frac{1}{\Omega}\int e^{iGx}e^{-iqh(x)}dx , \quad (5)$$

where Ω is the area of the unit cell. This is the eikonal[18] approximation, the hard-wall analog of the Born approximation, in the sense of being equivalent to a first-order expansion of the Green's function, G, of the form

$$G=G_0-\frac{\hbar^2}{2m}\int_{\text{surface}} G_0\vec{\nabla}G\cdot d\vec{S}$$

$$\simeq G_0-\frac{\hbar^2}{2m}\int_{\text{surface}} G_0\vec{\nabla}G_0\cdot d\vec{S} , \quad (6)$$

where G_0 is Green's function in the absence of the wall. Equation (5) is particularly useful for interpreting the scattering semiclassically. The integrand can be seen to be rapidly oscillating, and thus integrating to a small value, except in those regions for which

$$\frac{\partial h}{\partial x}\simeq\frac{-G}{q} . \quad (7)$$

Thus, as in classical scattering, particles deflect into an angle $\theta=\tan^{-1}(2G/q)$ when they strike the surface at a point where the slope is $\tan(\theta/2)$. At large q, the magnitude of this contribution to $|a_G|^2$ is properly proportional to the radius of curvature of the surface at the classical impact point. At small q, one has the additional effect of quantum-mechanical interference between reflections from points on the surface with identical slopes. This gives rise to beats in the diffraction pattern called supernumary rainbows.[18] The infinite radius of curvature at the inflection point always gives rise to a large peak in the diffraction pattern called the primary rainbow. This is typically the most distinct feature in the pattern.

The hard-wall appropriate for describing GaAs(110) is sufficiently corrugated that the eikonal[18] approximation describes scattering from it only qualitatively. In Fig. 2 we compare intensities of various diffracted beams as a function of polar angle of incidence for 21 meV ($\lambda=0.98$ Å) helium atoms scattering from a hard wall of the form

$$h(x)=h_0\cos(G_0x) , \quad (8)$$

where $G_0=1.125$ Å generates the reciprocal lattice

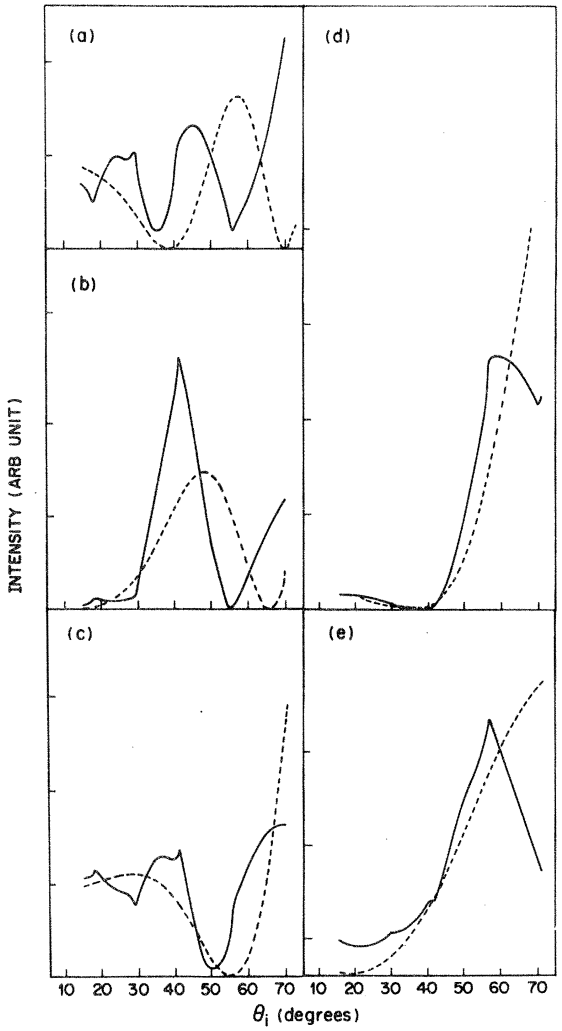

FIG. 2. Intensities of various diffracted beams for 21-meV helium atoms scattering from a hard wall described by Eq. (8) as calculated exactly (solid) and in the eikonal (Ref. 17) approximation (dashed), plotted versus θ_i, the polar angle of incidence of the probe. The specular beam is shown in (a) the first diffracted beam (deflected toward $\theta=0$) in (b), etc.

and $h_0=0.57$ Å is the corrugation parameter. The solid curve, calculated both by satisfying Eq. (3) at 30 points on the surface and by performing dynamic scattering calculations (see the Appendix) on a potential of the form

$$V(x,z)=e^{-\alpha[z-h(x)]}, \tag{9}$$

with $\alpha=12$ Å^{-1}, compares well with an eikonal calculation, shown as a dashed line, only for large deflection angles. The worst agreement is obtained for the specular beam [2(a)] in which the peak at 45° in the exact calculation is shifted to 55°, where a dip should occur. This would cause a 50% error if it were used to infer h_0 from specular scattering data. Also missing in the eikonal calculation are the sharp features at 17.9°, 28.3°, 40.5°, and 55.5°, which are thresholds[9] or resonances corresponding to selective adsorption into a state with zero binding energy, which occur when

$$\sin(\theta)=1-n\frac{\hbar}{\sqrt{2mE}}G_0=1-0.175n\ . \tag{10}$$

This discrepancy is less important, since these resonances will always reappear with the addition of an attractive well.

Softness of the wall has a significant effect on the diffraction pattern. In Fig. 3 we compare scattering calculations for a potential of the form of Eq. (9) for $\alpha=4.0$ and 8.0 Å^{-1}. We have plotted scattering intensity as a function of exit angle for various values of the incidence angle of the beam. For fairly normal incidence (bottom) the difference in α has little effect. In both cases one sees a primary and a supernumary rainbow displaced five and two beams from specular, respectively, which track with the specular beam as the incidence angle is increased. However, at large incidence angles, the collapse of first the supernumary and then the primary rainbow into the specular beam *occurs sooner for the softer wall.* This collapse is a consequence of shadowing by the ridges of the inflection point, the semiclassical source of the primary rainbow. Softness encourages collapse by causing the particle to refract outward as it skims across the tailing repulsive potential of the ridges, thus preventing it from reaching the inflection point. The tendency of softness to return intensity to the specular beam has been noted previously by Armand and Manson.[21]

One important aspect of rainbow scattering is that both the primary rainbow angle and the angle at which collapse occurs are independent of probe energy. Thus, in Fig. 4 we see that the same surface ($\alpha=4$) proved with 63 meV atoms also has a rainbow angle of 50° which collapses by 65° incidence. The fully developed pattern at 24.1° incidence shows three supernumary rainbows at 18°, 5°, and −12° which collapse in succession as the probe so lowered toward grazing incidence. One can also see emerging in Fig. 4 the outline of the U-shaped pattern characteristic[18] of classical scattering.

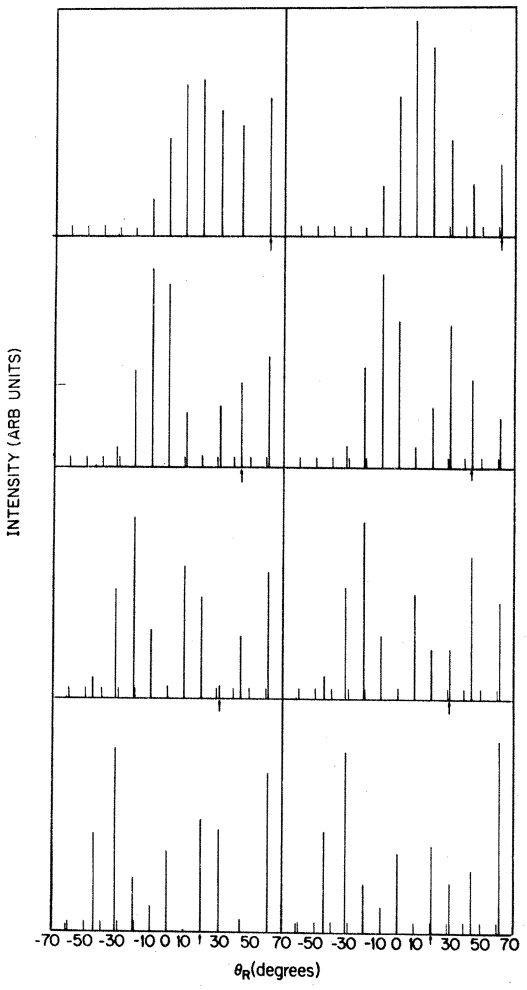

FIG. 3. Intensity plotted vs θ_R, the polar angle of exit of the probe, for various values of θ_i, the polar angle of incidence, for 21-meV helium atoms diffracting from a one-dimensional soft wall described by Eqs. (8) and (9) with $\alpha=4$ Å^{-1} (left) and $\alpha=8$ Å^{-1} (right). In each case, the arrow indicates the specular beam.

GaAs(110) has a slight asymmetry,[5] due either to the heteropolarity of the surface or to the reconstruction,[17] which manifests itself most distinctly as a difference in the left and right rainbow angles. In Fig. 5 we show the effect on the diffraction pattern of addition to $h(x)$ an asymmetry of the form

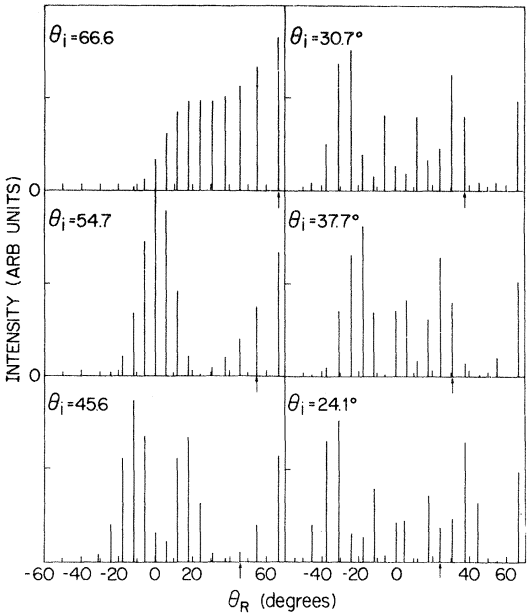

FIG. 4. Intensity plotted vs θ_R, the polar angle of exit of the probe, for various values of θ_i, the polar angle of incidence, for 63-meV helium atoms diffracting from a one-dimensional soft wall described by Eqs. (8) and (9) with $\alpha=4$ Å^{-1}. In each case, the arrow indicates the specular beam.

$$\Delta h(x)=h_1\sin(2G_0x)\ , \tag{11}$$

where $h_1=0.08$ Å. The small skewness this gives to h, shown to scale with and without Δh at the top, causes the rainbow angle for particles impinging on the steep side of the ridge (right) to be 60°, while that for particles impinging of the shallow side is 40°. As this is a net difference of 40% of the original of 50°, we conclude that a *small* asymmetry can produce *large* changes in the diffraction pattern.

III. DIFFRACTION FROM GaAs(110)

Up to effects due to the van der Waals attractive well on the surface, scattering from GaAs(110) (Ref. 5) is quantitatively that of the soft wall described by Eqs. (8) and (11). In Fig. 6 we compare experimental in-plane diffraction patterns across the troughs for 21 meV the atoms impinging at various polar angles θ_i. The left and right columns, which correspond to particles incident on the shallow and steep sides of the ridge, respectively, show the similarities and differences visible in the asymmetric soft-wall calculations of Fig. 5. In each case, one sees at fairly normal incidence

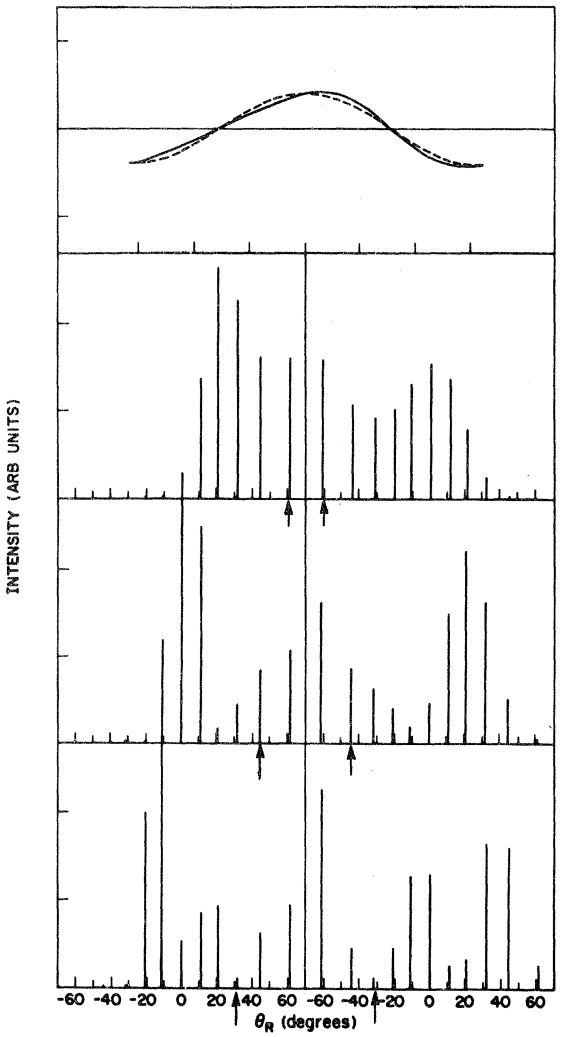

FIG. 5. Intensity plotted vs θ_R, the angle of exit of the probe, for various values of θ_i, the polar angle of incidence, for 21-meV helium atom diffracting from a one-dimensional asymmetric soft wall described by Eqs. (8), (9) and (11) with $\alpha=4$ Å^{-1}. The right column has been reflected across the center. The top shows drawings to scale of the classical turning-point surface with (solid) and without (dashed) the asymmetry described by Eq. (11).

($\theta_i=35°$) a bump at 14°, the supernumary rainbow, which collapses into the specular beam $\theta_i=45°$, and the entrance from the left at $\theta_i\sim 50°$ of a second feature, the primary rainbow, which collapses by $\theta_i\simeq 65°$. Although the collapse of rainbows occurs *sooner* in the left column than in the right, a result of wall asymmetry, similar behavior in Fig. 5 shows this asymmetry to be subtle and described well by Eq. (11). Thus, these data show GaAs(110) to be a smooth soft wall with a peak-

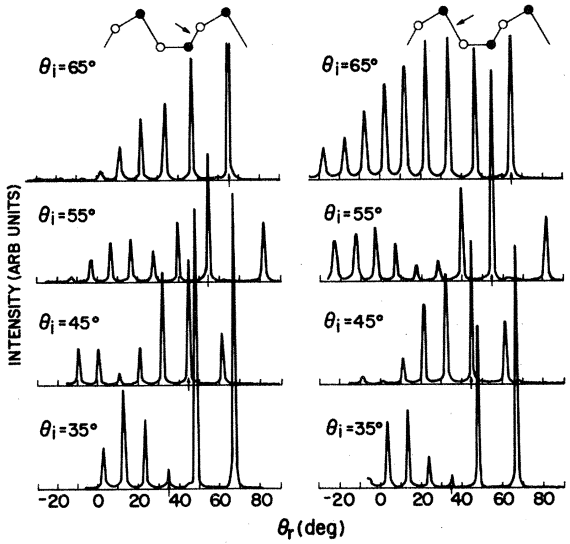

FIG. 6. Experimental in-plane diffraction patterns for 21-meV helium atoms beamed across the troughs of GaAs(110). Diffraction along the troughs cannot be seen in this scattering geometry. Intensity is plotted vs θ_R, the polar angle of exit of the probe, for various values of θ_i, the polar angle of incidence. The left and right columns correspond to particles impinging on the shallow and steep sides of the ridge, respectively. The arrow in each case indicates the specular beam. Note that data is not taken beyond $\theta_R = -20°$.

to-trough height of 1.1 Å and *an asymmetry which is small.* We emphasize that total collapse by $\theta_i \simeq 65°$ shows that the surface is soft.

Surface corrugation along the troughs has little effect on scattering across the troughs. This may be seen by considering a hard wall sufficiently smooth that its height function contains only first harmonics, in the manner

$$h(x,y) = h_x \cos(xG_x^0) + h_y \cos(yG_y^0) , \tag{12}$$

where G_x^0 and G_y^0 are the generators of the reciprocal lattice along and across the troughs, respectively. To the extent Eq. (5) is valid, the scattering amplitudes are redundant, in that they may be composed in the manner

$$\frac{1}{\Omega} \int e^{i\vec{G}\cdot\vec{r}} e^{-iqh(\vec{r})} d\vec{r}$$

$$= \frac{1}{\Omega} \left[\int e^{ixG_x} e^{-iqh_x} \cos(xG_x^0) dx \right]$$

$$\times \left[\int e^{iyG_y} e^{-iqh_y} \cos(yG_y^0) dy \right] , \tag{13}$$

and thus characterized by in-plane diffraction along principal directions only. The data in Fig. 6

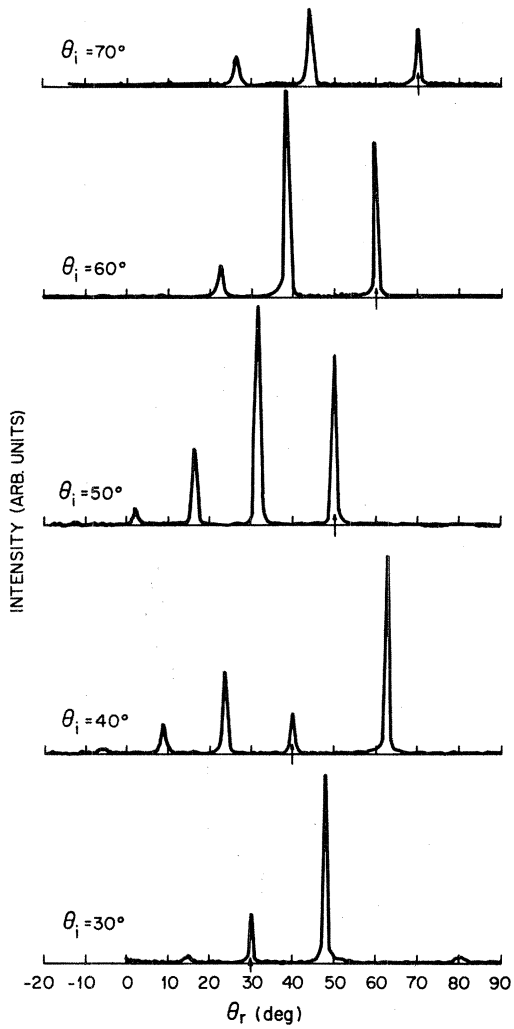

FIG. 7. Experimental in-plane diffraction patterns for 21-meV helium atoms beamed along the troughs of GaAs(110). Diffraction across the troughs cannot be seen in this scattering geometry. Intensity is plotted vs θ_R, the polar angle of exit of the probe, for various values of θ_i, the polar angle of incidence. The arrow in each case indicates the specular beam.

reflect only the y integral. If we probe the x integral by rotating the sample azimuthally 90° and perform the same experiment, we see, in Fig. 7, scattering power concentrated in the immediate vicinity of the specular beam, reflecting a corrugation parameter the order of $h_x \simeq 0.1$ Å, as is the case with many metals.[1] While it may be possible to fit these data with a one-dimensional hard-wall calculation, the approximate nature of the assumptions leading to separability in Eq. (13) would make such a fit unphysical. An experimental example of this problem is shown in Fig. 8, in which

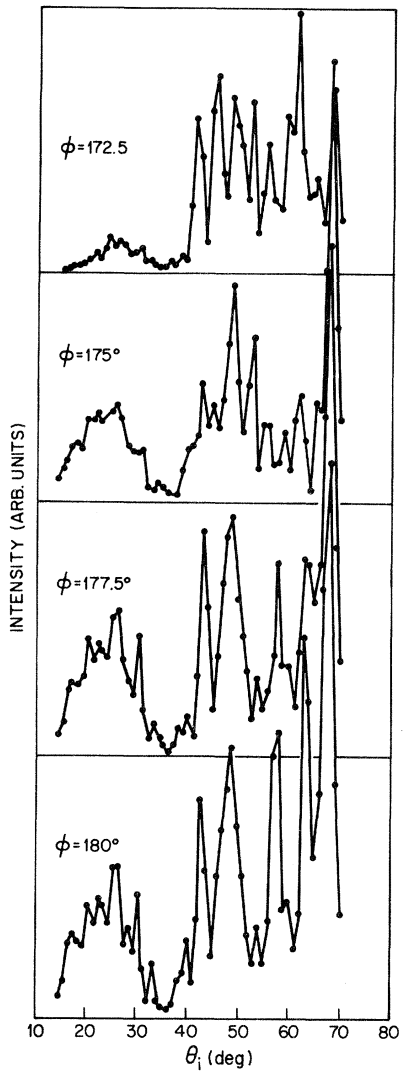

FIG. 8. Experimental specular intensity plotted vs θ_i, the angle of incidence of the probe, for various sample azimthus ϕ. The probe kinetic energy is 21 meV. $\phi=180°$ corresponds to scattering across the troughs (Fig. 6) and $\phi=0°$ corresponds to scattering along the trough (Fig. 7). Note the gradual destruction of the three-peak envelope as ϕ is decreased.

we reproduce the intensity of the specular beam as a function of polar angle of incidence for various sample azimuths. The evident azimuth dependence is inconsistent with Eq. (13), which predicts *no* azimuth dependence for $\vec{G}=0$. Variation of the reflection coefficient with azimuth involves a breakdown of the eikonal[18] approximation similar to that shown in Fig. 2, as well as the presence of higher fourier components in the height function absent in Eq. (12).

Each of the plots in Fig. 8 can be seen to have a distinct three-peak envelope with maxima at 25°, 45°, and 70°, in good agreement with the correct (solid line) hard-wall calculation in Fig. 1(a). (The peak at $\theta_i=58°$ is a resonance absent at $\phi=0$.) Since the specular scattering arises semiclassically from regions of the wall with zero slope, this envelope may be understood as being due to interference between probe particles reflected from the tops and bottoms of troughs. The dependence on polar angle θ occurs through the normal momentum transfer $q\simeq 2q_0\cos(\theta)$ in Eq. (5). If one approximates Eq. (5) as

$$a_0 \propto \cos(qh_0) , \tag{14}$$

one obtains a specular intensity curve similar to the dashed line in Fig. 2(a). The presence of an envelope in the GaAs data is important in that it indicates a van der Waals attractive well on the surface shallow compared with the kinetic energy of the probe. This is significant because a deep well tends to exaggerate the rainbow angle, and thus cause the surface to appear more corrugated than it actually is. The well depth is customarily[6–8] inferred from the positions of the selective-adsorption resonances, the fine structure in Fig. 8 absent in Fig. 2(a). However, we have found a self-consistent kinematic analysis of these data to be extremely difficult, as our scattering calculations have shown the resonance positions and intensities to be extremely sensitive to subtleties in the potential. We believe that band-structure effects[9] caused by the unusually large corrugation of this surface are responsible for the difficulty. Accordingly, rather than perform possible wrong kinematic analysis of the resonance positions, we have performed close-coupling scattering calculations (see the Appendix) on a series of model potentials and examined *trends* with increasing well depth. These potentials are of the form

$$V(x,y,z)=Ae^{-\alpha(z-h)}-Be^{-\alpha/3(z-h)}-C_{3/(z-z_0)^3} , \tag{15}$$

where

$$h=h_x\cos\left[\frac{2\pi x}{a}\right]+h_y\cos\left[\frac{2\pi y}{b}\right] . \tag{16}$$

The functional form of Eq. (15) is primarily a computational convenience. The parameters, listed in Table I, are chosen to optimize the 21-meV rainbows. The well depth is adjusted by varying B and z_0 only, as the effects of varying z_0 and C_3 are identical within the accuracy with which potentials

TABLE I. Parameters used in Eqs. (15) and (16) to generate Figs. 9 and 10. Distances are in Å and energies are in meV.

A	C_3	α	h_x	h_y	a	b
4.7×10^5	413	2.9	0.1	0.45	4.0	5.6

of the form of Eq. (15) scatter in agreement with experiment. In Fig. 9 the experimental (solid, top) specular scattering intensity of 21-meV He atoms beamed across the ridges as a function of polar angle is compared with that calculated from model potentials of the form of Eq. (15). Figure 9(a) ($B=0$, $C_3=0$) shows the distinct three-peak envelope evident in Fig. 2. The 1.5-meV depth of Fig. 9(b) ($B=0$, $z_0=-2.0$) can be seen to effectively bind one state giving rise to resonances corresponding well with features in the data. While resonances in the data are sufficiently numerous that this might be fortuitous, we think it is not, since any potential has one weakly bound state for which band-structure effects are small due to its distance from the surface. As the well depth is increased to 4 meV in Fig. 9(c) ($B=134$ and $z_0=1.23$) one sees the resonances in Fig. 9(b) moving to the *right* as their binding energy increases, and new resonances emerging at the old positions as new levels become bound. Band-structure effects may be the cause in Fig. 9(c) of the resonances at 26°, etc. lying to the left of the vacuum positions. In Fig. 9(d) ($B=202$ and $z_0=-0.5$) the attractive potential has been increased to force the most deeply bound state to resonate at 33°. We note that the envelope is beginning to be destroyed, and that there are large numbers of coincidences of resonance positions between theory and experiment. The rainbow angles of this potential still agree with experiment, up to the absence of asymmetry in Eq. (11). In Fig. 10, we compare across-trough diffraction patterns for the potentials generating Figs. 9(a) and 9(d). In each case, at $\theta_i=35°$ fully developed primary and supernumary rainbows can be seen at $-20°$ and 15°, respectively. As θ_i is increased, there is a definite trend for both to collapse, although in the presence of the attractive well (right) collapse is somewhat retarded.

The destruction of the specular beam envelope and the retardation of rainbow collapse are consequences of the presence of a deep attractive well seen in all our model calculations. We interpret the former as being due to the tendency of a deep well to dominate the momentum of the probe nor-

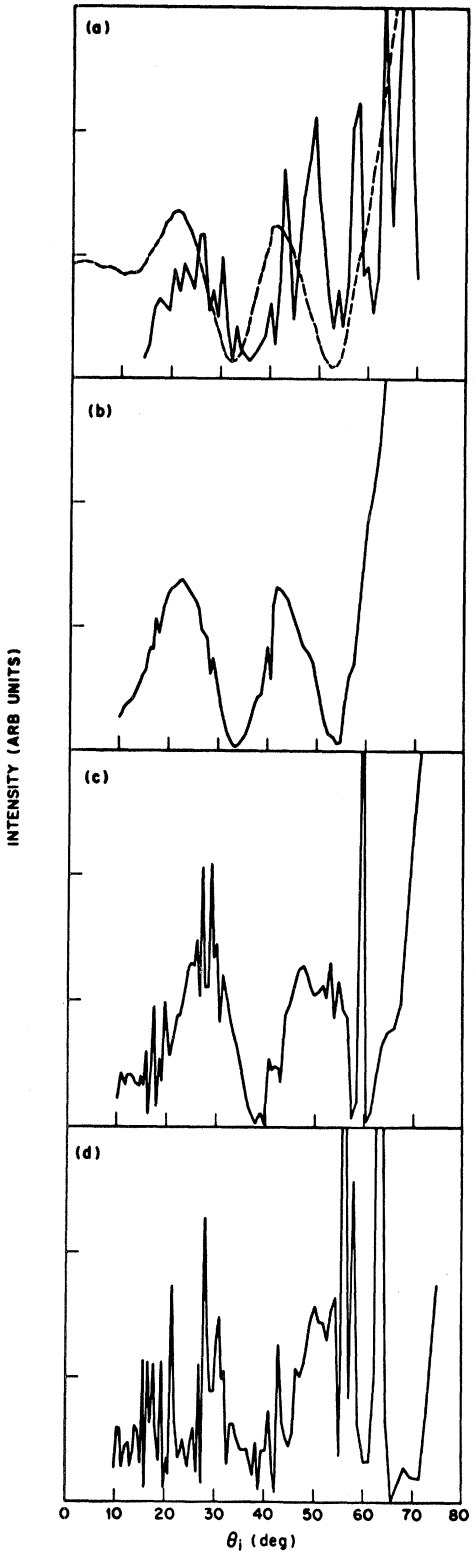

FIG. 9. Solid top: Experimental specular intensity plotted vs θ_i, the polar angle of incidence of the probe, for $\phi=180°$, reproduced from Figs. 8(a)–8(d); specular intensity calculated from potentials of the form of Eq. (15) with increasing attractive-well depth as described in the text.

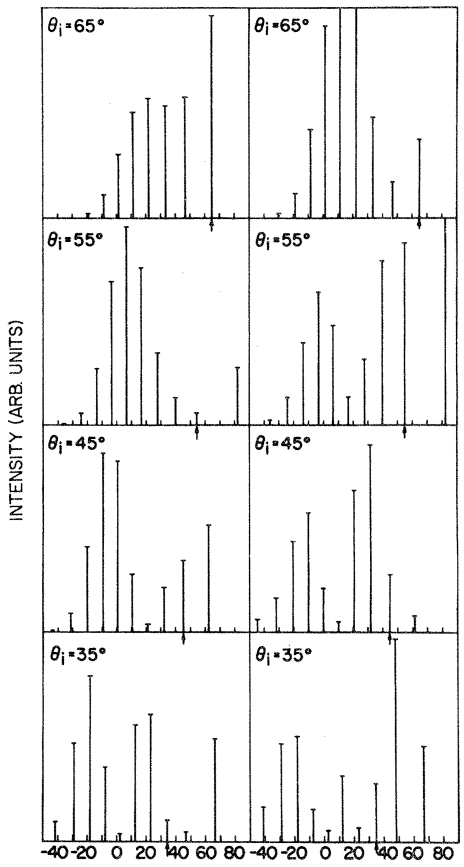

FIG. 10. Across-trough diffraction patterns calculated for a soft wall described by Eqs. (8) and (9) with $\alpha=3$ Å^{-1} (left) and for the potential generating Fig. 9(d) (right). The incident energy is 21 meV. Intensity is plotted vs θ_R, the polar angle of exit of the probe, for various values of θ_i, the polar angle of incidence. In each case, the arrow indicates the specular beam.

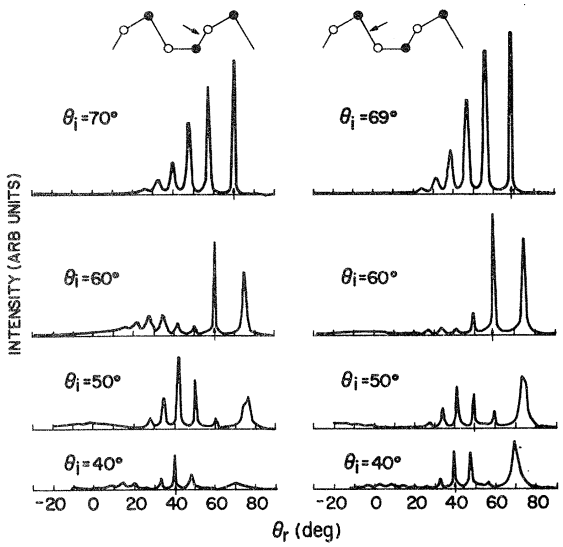

FIG. 11. Experimental in-plane diffraction patterns for 63-meV helium atoms beamed across the troughs of GaAs(110). Diffraction along the troughs cannot be seen in this scattering geometry. Intensity is plotted vs θ_R, the polar angle of exit of the probe, for various values of θ_i, the polar angle of incidence. In each case, the arrow indicates the specular beam.

mal to the surface at the classical turning point, and thus remove the dependence on θ_i. We believe failure to collapse to be caused by the tendency of the well to refract particles downward so that upon impact they are traveling at more normal incidence and thus become shadowed later. As we have found these calculations to be extremely sensitive to nuances in the potential, we venture to call agreement of Fig. 9(d) with experiment fair. More important are the *trends* with increasing well depth which preclude wells much deeper than the 7 meV of Fig. 9(d).

In Fig. 11, we show data taken with the same scattering geometry as in Fig. 5, but with a 63-meV ($\lambda=0.57$ Å) probe. Increased inelastic loss and instrumental broadening at large deflection angles causes agreement with the soft-wall calculation in Fig. 4 to be poor. Even so, vestiges of the rainbows seen in Fig. 4 (Ref. 5) can be seen to correctly emerge from the specular beam as the probe is raised toward more normal incidence. The primary rainbow can be seen in the left half of Fig. 11 to appear at $\theta_i=60°$ as a bump a 30°, which moves to 0° and then out of view as θ_i is decreased to 50° and 40°. In addition, the first supernumary rainbow may be seen developing at $\theta_i=50°$, and then forming a feature at 15° as θ_i is decreased to 40°. Similar behavior is seen in the right half of Fig. 11 except that rainbows emerge sooner as is the case in Fig. 6. In Fig. 12 we compare the specular intensity curve with that calculated using the potential generating Fig. 4. The calculation has been multiplied by $\cos(\theta_i)$ to account for diminution of the detector cross section at grazing incidence. While passing agreement of the peak positions at 41° and 54°, the overall agreement is poor, particularly at lower angles of incidence where the momentum transfer, and thus the inelastic losses, are greatest. It seems reasonable to speculate that the features between 60° and 90° are selective-adsorption resonances; however, considerably more work needs to be done before the 63-meV data is understood.

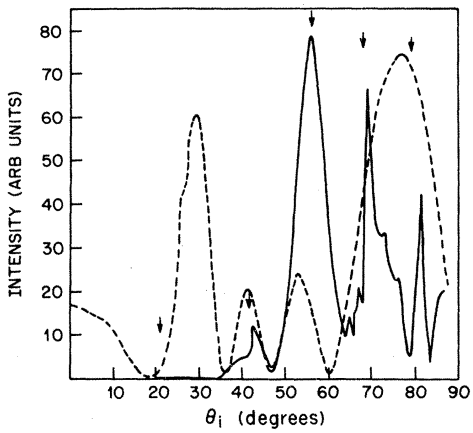

FIG. 12. Solid: Experimental specular intensity plotted vs θ_i, the polar angle of incidence of the probe, for $\phi=180°$ (probe beamed across the troughs). The probe kinetic energy is 63 meV. Dashed: Specular intensity calculated for a one-dimensional soft wall described by Eqs. (8) and (9) with $\alpha=4$ Å^{-1}. This potential also generated Fig. 4.

IV. GENERATING A POTENTIAL

It has been possible[14] for many years to compute fairly accurate van der Waals potentials between closed-shell atoms and molecules. In light of this, it is somewhat surprising that there has never been a successful first-principles calculation of a potential between a helium atom and an insulator. In this section, we examine the reasons for this and propose methods of overcoming them which are not unworkably complex, and yet which can provide a reasonable interpretation of the GaAs data.

Of the equivalent methods presently available for calculating atom-atom potentials, the simplest is the Gordon-Kim technique.[14] This method is based on the observation that Hartree-Fock calculations for the He-He system at typical van der Waals separations produce a charge density equal within 10% to a superposition of atomic He charge densities. The method involves computing the total electronic energy in the local density-functional approximation, using the sum of target and probe charge densities for ρ, and relying on the nonlinearities of the functional to provide the interaction. The local density expression for E takes the form

$$E=T+V_{ei}+V_{ee}+V_{ii}+V_{xc}\ , \tag{17}$$

where

$$T=\tfrac{3}{10}(3\pi^2)^{2/3}\frac{\hbar^2}{m}\int\rho^{5/3}(\vec{r})d\vec{r} \tag{18}$$

is the kinetic energy,

$$V_{ei}=-\sum_j Z_j e^2\int\frac{\rho(\vec{r})}{|\vec{r}-\vec{R}_j|}d\vec{r} \tag{19}$$

is the electron-ion interaction, with Z_j the charge on the ion at $\vec{R}_j$,

$$V_{ee}=\tfrac{1}{2}e^2\int\int\frac{\rho(\vec{r})\rho(\vec{r}')}{|\vec{r}-\vec{r}'|}d\vec{r}\,d\vec{r}' \tag{20}$$

is the electron-electron interaction,

$$V_{ii}=\tfrac{1}{2}\sum_{jj'}\frac{Z_jZ_j'e^2}{|\vec{R}_j-\vec{R}_j'|} \tag{21}$$

is the ion-ion interaction, and

$$V_{xc}=\frac{-3}{4}\left[\frac{3}{\pi}\right]^{1/3}e^2\int\rho^{4/3(\vec{r})d\vec{r}}+\int\rho(\vec{r})F(r_s)d\vec{r} \tag{22}$$

is the contribution from exchange and correlation. The small correlation correction on the right of Eq. (22) is given in terms of $r_s=me^2/\hbar^2(3/4\pi\rho)^{1/3}$ as

$$F(r_s)\simeq\frac{me^4}{\hbar^2}(-0.438r_x^4+1.325r_s^{-3/2}-1.47r_s^{-2}-0.4r_s^{-5/2}) \tag{23}$$

for $r_s\lesssim 1$, and

$$F(r_s)\simeq\frac{me^4}{\hbar^2}[0.0311\ln(r_s)-0.048+0.009r_s\ln(r_s)-0.01r_s]\ , \tag{24}$$

for $r_s\gtrsim 1$. The region of relevant charge densities spans the region of $r_s=1$. Using Clementi functions[22] to generate charge densities for the rare gases, Gordon and Kim[14] succeeded in producing potentials between rare-gas atoms other than He agreeing with experiment to roughly 2% in the position of the potential minimum and to roughly 15% in the depth of the minimum. Potentials involving He typically differed from experiment by 20% in the position of the minimum and 80% in its depth. These errors were attributed[14] to the incorrectness of statistical exchange and correlation for atoms with very few electrons. The potential

minimum for He-He has been reproduced by a configuration-interaction calculation,[23] which automatically includes correlation energies correctly, and thus it can be calculated if sufficient effort is expended. Such a calculation is not practical for surfaces.

The Gordon-Kim method has been used by Freeman[13] to calculate the interaction between rare gases and graphite. Using Hartree-Fock charge densities for the probe and target, Freeman reports attractive-well depths, for all gases except Xe, 0.5 (He) to 0.25 (Kr) times the value determined from experiment by Steele.[24] Freeman attributes this disparity partly to absence of dispersion forces (improper estimation of correlation by the density functional) and partly to inaccuracies in the graphite charge density far away from the surface. We note that the error in the well depth is systematically positive, as would be expected for missing dispersion forces, while the He-He potential of Gordon and Kim[14] is four times too deep, i.e., the nature of the error is different in the two cases. Better agreement with experiment in the case of He-LiF was obtained by Tsuchida,[15] who represented the potential as a sum of two-center He-Li^+ and He-F^- components, estimated to be identical to the known He-He and He-Ne potentials. Tsuchida reported an attractive-well depth only 12% deeper than that determined experimentally and a peak-to-valley distance of the equivalent hard wall of 0.34 Å compared to 0.54 Å estimated from diffraction intensities by Boato *et al.*[6] Carlos *et al.*[11] have compared matrix elements of this potential between bound states of its lateral average to those inferred from selective-adsorption splittings and found the theoretical values up to a factor of 2 too large. They attribute this discrepancy to errors in the sizes of the ions incurred in substituting the rare-gas potentials.

The persistent tendency of the local-density-functional method to underestimate the depth of the He-target attractive well for both atoms and solids, while apparently being adequate for other probes,[14] suggests that *van der Waals potentials involving helium are significantly different from those of other closed-shell atoms.* The anomalous behavior of helium is due primarily to the smallness of its radius $a_0=0.313$ Å. This causes the major contribution to the interaction energy in Eqs. (15)–(20) to come from the presence of the tenuous tails of target charge density at the helium core, rather than from the bonding region, as in the case[14] with other rare gases. Another consequence is that when the probe is within a van der Waals distance of the target, its electrons are rarely close to the target, and thus a proper exchange-correlation hole rarely forms about them.[25] For sufficiently large target-probe separations, this latter effect always causes a breakdown of the local density expression for the exchange-correlation energy, manifested as the inability of the method to correctly reproduce the $1/r^6$ dispersion energy.

In the remaining discussion we shall assume that local-density approach for helium has only two faults: (1) The local expression for the correlation energy is *never* valid at the separations of interest, (2) the highly correlated nature of the He ground state makes the remaining components of the potential difficult to evaluate *accurately*. Our procedure for circumventing these problems will be to parametrize the part of the potential *not* due to correlation and then to add this to the ordinary $1/r^6$ nonlocal expression for the correlation energy at "large" separation. We emphasize that this approach is valid only because helium is small.

We begin by observing that, in the case of Ar-Ar, the kinetic, Coulomb, and exchange contributions to the Gordon-Kim potential are comparable and tend to scale with one another at interatomic separations of interest to that the order of the potential can be estimated from the kinetic energy alone. This observation does not apply at large separations, where the correlation energy dominates. Since the interaction arises near the He nucleus, one can expand Eq. (18) in the manner

$$\int [(\rho_{\rm He}+\rho_{\rm target})^{5/3}-\rho_{\rm He}^{5/3}-\rho_{\rm target}^{5/3}] \simeq \tfrac{5}{3}\int \rho_{\rm He}^{2/3}\rho_{\rm target}\,, \quad (25)$$

which in the limit of uniform $\rho_{\rm target}$ reduces to a rule of the form

$$V\simeq T\rho_{\rm target}\,, \quad (26)$$

with $\rho_{\rm target}$ evaluated at the He nucleus and T given in terms of the He charge density

$$\rho_{\rm He}(r)=\frac{2}{\pi a_0 3}e^{-2r/a_0} \quad (27)$$

by

$$T=\tfrac{1}{2}(3\pi^2)^{2/3}\frac{\hbar^2}{m}\int \rho_{\rm He}^{2/3}=\tfrac{1}{6}(6\pi)^{5/3}\left[\frac{\hbar^2}{me}\right]^2 =9.0\times 10^4\ \text{meV Å}^3\,, \quad (28)$$

where $a_0=\frac{16}{27}(\hbar^2/me^2)$ is the He radius. Equation (26) is identical to a rule proposed recently by Esjberg and Nørskov,[16] their value of T (1.1×10^5 meV Å^3) likewise being derived from calculations of the energy to embed a helium atom in a uniform electron gas of density ρ_{target}. For the present purposes, Eq. (26) with this value of T is meant only as a rough guide. The approximations involved in obtaining it include ignoring the Coulomb and exchange-correlation contributions [Eqs. (19)–(22)], which tends to increase T, and the assumption of uniformity, which tends to reduce it. To estimate the size of the latter effect, we approximate ρ_{target} in the vicinity of the probe by

$$\rho_{\text{target}}\simeq\rho_0 e^{-\alpha z}, \tag{29}$$

and replace the exponent $\frac{5}{3}$ in Eq. (25) by 2, to obtain a dilation factor f for T given by

$$f=\left[1-\left[\frac{\alpha a_0}{2}\right]^2\right]^{-2}=1.65, \tag{30}$$

for $\alpha=3$ Å^{-1}, a representative value for solids. We note that errors in T of this order will affect the repulsive potential minimally, since the exponential form of Eq. (29) causes f to displace the classical turning point a distance Δr given by

$$\Delta r=\frac{1}{\alpha}\ln(f)=0.17\text{ Å}. \tag{31}$$

Because of the large size of T, great care must be taken in Eq. (26) to use a ρ_{target} accurate in the tails. If, for example, one uses the charge density of Herman and Skillman[26] for atomic Ar, one obtains (with $T=1.0\times10^5$ meV Å^3) a classical turning point for He-Ar potential of 2.3 Å, as opposed to the experimental value of 2.7 Å. The disparity comes from the use of Slaters's value of $\alpha=1$ in the exchange-correlation potential

$$V_{\text{xc}}(\vec{r})=\frac{3\alpha}{2}\left[\frac{3}{\pi}\right]^{1/3}\rho^{1/3}(\vec{r}), \tag{32}$$

rather than the Kohn-Sham value of a $\alpha=\frac{2}{3}$, which is more suitable for describing ground-state properties of multielectron atoms. These two values of α generate eigenvalues for the Ar $3p$ state of $E_1=0.53$ and $E_2=0.38$ hartrees, respectively, and these give rise to different exponential decays of the form

$$\rho(r)\simeq\rho_0\exp\left[-\beta\frac{2}{\hbar}\sqrt{2mE}\,r\right], \tag{33}$$

with $\beta\simeq1.21$ arising from the sphericity of the wave function. Thus, the different classical turning points R_1 and R_2 related by

$$\frac{R_1}{R_2}\left[\frac{E_2}{E_1}\right]^{1/2}=0.85. \tag{34}$$

We note that the Kohn-Sham value of α is commonly used in electronic structure calculations for surfaces, in part because it gives better work functions.

The exponential character of atomic wave functions at typical van der Waals distances is shown in Fig. 13, in which theoretical charge densities, calculated using Wigner exchange[27] (α variable and $\simeq\frac{2}{3}$ in regions of large charge density) for all the rate gases except He and for Ga $4s^2 4p$ and As $4s^2 4p^3$ are plotted. The dashed line indicates the classical turning point of 21-meV helium atoms, assuming Eq. (26) with $T=1.0\times10^5$ meV Å. These are compared with the experimental

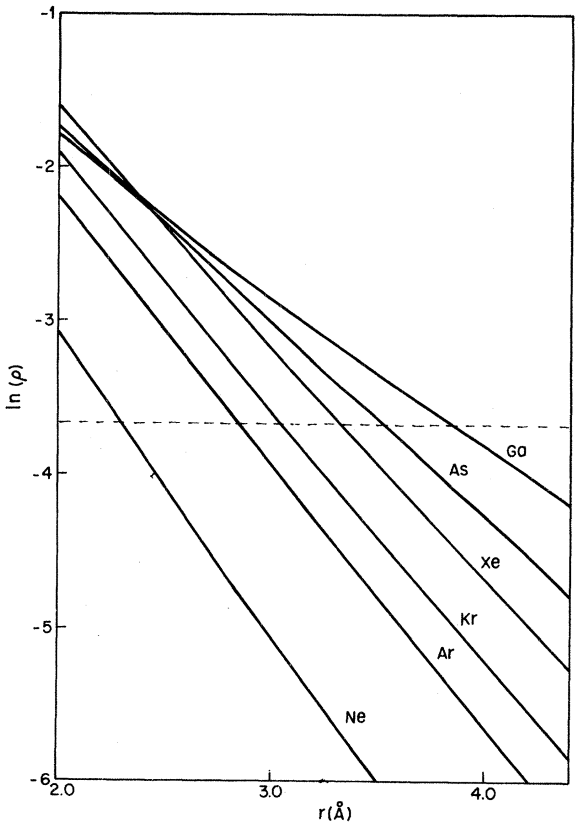

FIG. 13. Valence-charge density vs distance from the nucleus for several atoms, calculated using Wigner exchange as described in the text. The dashed line indicates the classical turning-point separation for 21-meV helium atoms, as calculated from Eq. (26) using $T=1.0\times10^5$ meV Å^3. The units of ρ are Å^{-3}.

TABLE II. Distance of closest approach, R^{CTP}, for 21-meV helium atoms impinging on various atomic targets, as calculated using Eq. (26), compared with experimental values of Chen *et al.* (Ref. 28). Also shown are the logarithmic derivitive of ρ at the turning point, the one-dimensional decay parameter associated with the eigenvalue of the outermost p electron, β the ratio of these used in Eq. (33), and f as defined in Eq. (30).

	$R^{\mathrm{CTP}}_{\mathrm{theor}}$	$R^{\mathrm{CTP}}_{\mathrm{expt}}$	$\frac{\partial}{\partial r}\ln(\rho)$	$\frac{2}{\hbar}\sqrt{2mE}$	β	f
Ga	3.83		2.09	1.71	1.22	1.25
As	3.51		2.87	2.35	1.22	1.56
Xe	3.32	3.17	3.43	2.93	1.18	1.66
Kr	3.04	2.87	3.70	3.09	1.19	1.84
Ar	2.83	2.72	3.89	3.24	1.20	2.01
Ne	2.29 (2.44)	2.27	4.60	3.69	1.19	2.64

values of Chen *et al.*,[28] in the left-hand columns of Table II. For Ar, Kr, and Xe, the theoretical turning point is 0.11 to 0.17 Å larger than the experimental one, as would be expected in the absence of dispersion forces. The theoretical Ne turning point is only 0.02 Å larger than the experimental one. This is probably caused by an excessively negative Ne $2p$ eigenvalue, due to the inadequacy of statistical exchange in an atom with very few electrons, although a contributing factor may be the inhomogeneity factor f approximated by Eq. (32). A reduction of this eigenvalue from 13.3 to 11.7 eV or a dialation of ρ_{Ne} or T by 2.0 would increase this distance to 2.49 Å (shown in parentheses in Table I) to be more in line with the other rare gases.

For all rare-gas targets except He and Ne, the C_6/r^6 dipole dispersion energy calculated with published[29,30] values for C_6, when added to the repulsive potential generated by Eq. (26) in the manner

$$V \simeq T\rho_{\mathrm{target}} - C_6/r^6 , \tag{35}$$

produces a potential minimum at r_m of depth ϵ_m agreeing with experiments within 4% and to within a factor of 2, respectively. A comparison of the experimental and theoretical 21-meV classical turning points and attractive-well parameters is shown in Table III. Similar agreement may be seen to occur for Ne if the enhanced repulsion is used (producing the values in parentheses). Even with enhanced Ne repulsion all four targets may be seen to have inadequately deep attractive wells. Noting that the magnitude of the error is the same in all cases, even though the quadrupole polarizabilities are known[30] to vary by a factor of 20 from Ne to Xe, we postulate that the *total* missing energy, primarily Coulomb, and exchange-correlation energy not proportional to ρ_{target} or included in the dipole dispersion energy, is approximately local, and thus

TABLE III. Separation r_m at the potential minimum, the value ϵ_m of this minimum, and the classical turning-point separation R^{CTP} for 21-meV helium atoms impinging on various rare-gas targets, as calculated using Eq. (35), compared with experimental values of Chen *et al.* (Ref. 28). The Ne values in parentheses are calculated using an enhanced repulsion, as discussed in the text.

	r_m^{theor}	r_m^{expt}	$\epsilon_m^{\mathrm{theor}}$	$\epsilon_m^{\mathrm{expt}}$	$R^{\mathrm{CTP}}_{\mathrm{theor}}$	$R^{\mathrm{CTP}}_{\mathrm{expt}}$
Xe	4.3	4.15	1.04	2.17	3.20	3.17
Kr	3.9	3.75	1.28	2.13	2.92	2.87
Ar	3.6	3.54	1.53	2.08	2.70	2.72
Ne	2.9 (3.2)	3.21	1.62 (0.97)	1.23	2.13 (2.37)	2.27

TABLE IV. Separation r_m at the potential minimum, the value ϵ_m of this minimum, and the classical turning-point separation R^{CTP} for 21-meV helium atoms impinging on various rare-gas targets, as calculated using Eq. (36), compared with experimental values of Chen *et al.* (Ref. 28). The Ne values in parentheses are calculated using an enhanced repulsion as discussed in the text. The Ar value in parentheses is that of Aziz *et al.* (Ref. 31).

	r_m^{theor}	r_m^{expt}	$\epsilon_m^{\mathrm{theor}}$	$\epsilon_m^{\mathrm{expt}}$	$R^{\mathrm{CTP}}_{\mathrm{theor}}$	$R^{\mathrm{CTP}}_{\mathrm{expt}}$
Xe	4.2	4.15	1.89	2.17	3.17	3.17
Kr	3.8	3.75	2.19	2.13	2.90	2.87
Ar	3.5	3.54	2.50	2.08 (2.59)	2.67	2.72
Ne	2.8 (3.1)	3.21	2.69 (1.80)	1.23	2.10 (2.37)	2.27

can be included empirically by modifying the functional in ρ_{target} to include a short-range attraction which does not overwhelm either the repulsion at short distances or the dispersion energy at large ones. This may be accomplished by subtracting a term proportional to $\rho_{\mathrm{target}}^{\gamma}$ where $\gamma<1$. We find the value $\gamma=\frac{1}{3}$ to be adequate, although the exact value is not crucial. Thus, we propose a rule of the form

$$V=T\rho_{\mathrm{target}}-X\rho_{\mathrm{target}}^{1/3}-C_6/r^6\,, \tag{36}$$

where $T=1.0\times10^5$ meV Å^3 and $X=40.0$ meV Å are universal constants selected to optimize the fit to the rare gases.

We note that Eq. (36) is automatically consistent with Tsuchida's[15] result for LiF, since atomic charge densities and polarizabilities are known to be approximately additive in ionic solids, and since $\rho_{\mathrm{target}}^{1/3}$ is usually dominated by one atom or the other, and is thus also additive. The agreement between potentials generated by Eq. (36) for rare-gas targets and the experimental potentials of Chen *et al.*[28] is summarized in Table IV. For all targets except Ne, r_m, ϵ_m, and R^{CTP} agree to within 1.5%, 18%, and 2%, respectively, tolerances similar to those obtained by the Gordon-Kim technique[14] for heavier rare-gas probes. Tolerances for Ne are somewhat poorer (3.5%, 17%, and 4%). Considerably better agreement (1%, 1%, and 3%) is obtained for Ar if the experimental potential of Aziz *et al.*[31] is used for comparison. We note that the experimental trend for the well depth to increase with the atomic number of the target is not observed in the theory. This suggests that the attraction absent from Eq. (35) is not completely local, but tends to increase with the target polarizability. However, since the remaining error (0.28 meV for Xe) is small compared with the kinetic energy of the probe, and since the Xe polarizability is about half that of an atom in a typical semiconductor, we argue that this error will be negligible in semiconductors. The difficulty of observing errors of this order experimentally is demonstrated by the inability of Keil *et al.*[32] and Aziz *et al.*[31] to agree on the He-Ar well depth to better than 30%.

While the transfer of the local part of Eq. (28) to a surface is straightforward, transfer of the dispersion energy is subtle. Unlike a rare-gas target, a solid is much larger than the target-probe separation, it has a continuous distribution of electronic levels, and its charge is inhomogeneously distributed. Assuming for the moment that screening is negligible (this is not generally the case), we write for the interaction energy $\Delta\epsilon_c$ due to correlation as

TABLE V. Values of C_6 calculated using Eq. (40) compared with those reported by Dalgarno (Ref. 29). $\bar{E}^{\mathrm{ionization}}$ is the first ionization energy and $\bar{E}^{\mathrm{Dalgarno}}$ is the single-oscillator excitation energy calculated from C_6 (Ref. 29) using Eq. (40).

	$\bar{E}^{\mathrm{ionization}}$	$C_6^{\mathrm{ionization}}$	C_6^{Dalgarno}	$\bar{E}^{\mathrm{Dalgarno}}$
Xe	12.1	1.11	1.12	12.0
Kr	14.0	0.93	0.77	16.2
Ar	15.8	0.80	0.57	20.2
Ne	21.6	0.52	0.18	44.8

$$\Delta\epsilon_c = e^4 \sum_{\substack{fi \\ \text{target}}} \sum_{\substack{f'i' \\ \text{probe}}} \left| \int\int \frac{\psi_{f'}(\vec{r}\,')\psi_{i'}(\vec{r}\,')\psi_f(\vec{r})\psi_i(\vec{r})}{|\vec{r}-\vec{r}\,'|} d\vec{r}\, d\vec{r}\,' \right|^2 \Big/ [(E_f - E_i) + (E_{f'} - E_{i'})] \,, \tag{37}$$

where the sums run over filled and empty states of the target and probe separately. Equation (37) can be evaluated conveniently using the single-oscillator approximation, valid to the extent that the excitation energies contributing significantly lie near one value. Approximating $E_f - E_i$ by $\bar{E}$ for these transitions, we have

$$\Delta\epsilon_c \simeq \frac{e^4}{(\bar{E}+\bar{E}')} \frac{1}{\bar{E}\bar{E}'} \sum_{\substack{fi \\ \text{target}}} \sum_{\substack{f'i' \\ \text{probe}}} (E_f - E_i)(E_{f'} - E_{i'}) \left| \int\int \frac{\psi_{f'}(\vec{r}\,')\psi_{i'}(\vec{r}\,')\psi_f(\vec{r})\psi_i(\vec{r})\, d\vec{r}\, d\vec{r}\,'}{|\vec{r}-\vec{r}\,'|} \right|^2 . \tag{38}$$

This may be evaluated using the f sum rule to obtain

$$\Delta\epsilon_c \simeq 6 \left[\frac{\hbar^2 e^2}{2m} \right]^2 \frac{1}{(\bar{E}+\bar{E}')} \frac{1}{\bar{E}\bar{E}'} \int\int \frac{\rho_{\text{target}}(\vec{r})\rho_{\text{probe}}(\vec{r}\,')}{|\vec{r}-\vec{r}\,'|^6} \,, \tag{39}$$

which is the well-known London formula.[1] The integral in Eq. (39) is divergent if there is any nonzero overlap of ρ_{target} and ρ_{probe}. If there were none, and if the target and probe were well separated, then we could write

$$\Delta\epsilon_c \simeq 6 \left[\frac{\hbar^2 e^2}{2m} \right]^2 \frac{1}{(\bar{E}+\bar{E}')} \frac{1}{\bar{E}\bar{E}'} N' \sum_j \frac{N_j}{r_j^6} \,, \tag{40}$$

where $N_2' = 2$ is the number of electrons in the probe and N_j is the number of valence electrons on the jth target atom separated from the probe by distance r_j. Assuming that Eq. (40) is approximately correct, it may be tested against the rare-gas targets using the empirical observation[29] that most of the dipole-oscillator strength for the p electrons resides near the atom's ionization energy. Thus, in Table V, we compare C_6, the coefficient of $1/r^6$, as reported by Dalgarno[29] with the value calculated from Eq. (40) using the ionization energy for $\bar{E}$, a value of 34.6 eV for $\bar{E}'$, picked to given the correct[29] value of C_6 for He-He, and $N=6$ p electrons. Agreement for all targets except Ne is within 30% and that for Ne is within a factor of 2. The noticeable tendency of the theory to overestimate C_6, particularly for smaller atoms, derives from the crudeness of the estimate for $\bar{E}$, which tends to be slightly higher than the ionization energy. For example, the known[33] He dc polarizability $\alpha(0)$ is 0.195 Å^3, compared with values of 0.188 and 0.095 Å^3 calculated from the single-oscillator model in the manner

$$\alpha(0) \simeq 2 \frac{e^2\hbar^2}{m\bar{E}'^2} \,, \tag{41}$$

with $\bar{E}'$ set equal to 34.6 and 24.6 eV, the ionization energy, respectively.

The divergence in Eq. (39) is a pathology of the single-oscillator approximation stemming from its tendency to overemphasize high-energy excitations of the target. This tendency is not important when the dipole approximation is valid because the dipole matrix element cuts out high-energy contributions to Eq. (38) sufficiently rapidly to nullify the effect of multiplying by ϵ_{fi}. The full Coulomb interaction does not have this property, however, and thus Eq. (39) is a bad approximation, in that it tends to exaggerate the severity of singularity at $\vec{r}=\vec{r}\,'$. In a better approximation, we replace the excited states by plane waves $|q\rangle$ of excitation energy $E + \hbar^2 q^2/2m$, we write

$$\sum_f \left\langle i \left| \frac{1}{|\vec{r}-\vec{r}\,'|} \right| f \right\rangle \left\langle f \left| \frac{1}{|\vec{r}-\vec{r}\,'|} \right| i \right\rangle \simeq \sum_q \left\langle i \left| \frac{1}{|\vec{r}-\vec{r}\,'|} \right| q \right\rangle \frac{1}{\bar{E}+\hbar^2 q^2/2m} \left\langle q \left| \left[H, \frac{1}{|\vec{r}-\vec{r}\,'|} \right] \right| i \right\rangle$$

$$= \frac{1}{\bar{E}} \left\langle i \left| \frac{1}{|\vec{r}-\vec{r}\,'|} \Pi^2 \left[H, \frac{1}{|\vec{r}-\vec{r}\,'|} \right] \right| i \right\rangle , \tag{42}$$

where Π is a smoothing operator given by

$$\Pi=\sum_q \left[\frac{E}{\bar{E}+\hbar^2q^2/2m}\right]^{1/2} |q\rangle\langle q| \ . \tag{43}$$

Since Π commutes with the kinetic energy operator T, and since

$$\Pi|i\rangle\simeq|i\rangle \ , \tag{44}$$

one has

$$\left\langle i\left|\frac{1}{|\vec{r}-\vec{r}'|}\Pi^2\left[H,\frac{1}{|\vec{r}-\vec{r}'|}\right]\right|i\right\rangle\simeq\left\langle i\left|\left[\Pi\frac{1}{|\vec{r}-\vec{r}'|}\Pi\right]\left[T,\left[\Pi\frac{1}{|\vec{r}-\vec{r}'|}\right]\right]\right|\right\rangle . \tag{45}$$

Thus, we modify Eq. (39) with the substitution

$$\frac{1}{|\vec{r}-\vec{r}'|}\rightarrow\Pi\frac{1}{|\vec{r}-\vec{r}'|}\Pi=\frac{1-e^{\lambda|\vec{r}-\vec{r}'|}}{|\vec{r}-\vec{r}'|} \ , \tag{46}$$

with

$$\frac{\hbar^2\lambda^2}{2m}=\bar{E} \tag{47}$$

to obtain

$$\Delta\epsilon_{\text{correlation}}\simeq 6\left[\frac{\hbar^2e^2}{2m}\right]^2\frac{1}{(\bar{E}+\bar{E}')}\frac{1}{\bar{E}\bar{E}'}\int\int\rho_{\text{target}}(\vec{r})\rho_{\text{probe}}(\vec{r}')\lambda^6F(\lambda|\vec{r}-\vec{r}'|)d\vec{r}\,d\vec{r} \ , \tag{48}$$

where

$$F(|\vec{r}|)=\tfrac{1}{6}\sum_{jk}\left|\frac{\partial}{\partial x_j}\frac{\partial}{\partial x_k}\left[\frac{1-e^{|\vec{r}|}}{|\vec{r}|}\right]\right|^2 . \tag{49}$$

A comparison of $x^2F(x)$ and $1/x^4$ is shown in Fig. 14. We note that $F(x)$ converges to $1/x^6$ at large x, but that it diverges only as $1/x^2$ for small x, and thus does not produce infinite interactions.

To test Eq. (48), we adopt a rare-gas potential analogous to Eq. (36) of the form

$$V(\vec{r}')=T\rho_{\text{target}}(\vec{r}')-X\rho_{\text{target}}^{1/3}(\vec{r}')-6\left[\frac{\hbar^2e^2}{2m}\right]^2\frac{1}{(\bar{E}+\bar{E}')}\frac{1}{\bar{E}\bar{E}'}2\lambda^6\int\rho_{\text{target}}(\vec{r}')F(\lambda|\vec{r}-\vec{r}'|)d\vec{r}' \tag{50}$$

with $\bar{E}$ chosen to given the correct value of C_6 and with λ treated as a variable into which to absorb approximation errors from Eqs. (42)–(45). Agreement is optimized with X set to 30 meV Å. We take ρ_{target} within the integral to be of the form

$$\rho_{\text{target}}(\vec{r}')=Ae^{-\beta|\vec{r}|} \ , \tag{51}$$

with β and A chosen to agree with Fig. 13 at $|\vec{r}|=3.5$ Å and to normalize the total charge to six electrons. With this approximation we find that the values of λ (1.8 Å^{-1} and larger) given by Eq. (47) are too large, but that essential agreement with Eq. (36) can be obtained using the universal value of $\lambda=1.35$ Å^{-1}. The agreement with experiment of potentials generated using Eq. (50) with this value of λ is summarized in Table VI, which is the analog of Table III.

The removal of the $1/r^6$ divergence in Eq. (39) is intimately related to the momentum-dependent nature[34] the dielectric function of the target, its inability to screen at short distances for frequencies $\hbar\omega\lesssim\bar{E}$. In particular, the potential at $\vec{r}'$ resulting from injecting unit charge at $\vec{r}'$ at frequency ω, given by

$$\sum_f\frac{2\epsilon_{fi}}{(\hbar\omega)^2-\epsilon_{fi}^2}\left\langle i\left|\frac{1}{|\vec{r}-\vec{r}'|}\right|f\right\rangle\left\langle f\left|\frac{1}{|\vec{r}-\vec{r}'|}\right|i\right\rangle , \tag{52}$$

can be evaluated at $\omega=0$ as

TABLE VI. Separation r_m at the potential minimum, the value ϵ_m of this minimum, and the classical turning-point separation $R^{\rm CTP}$ for 21-meV helium atoms impinging on various rare-gas targets, as calculated using Eq. (50) with $X=30$ meV Å compared with experimental values of Chen *et al.* (Ref. 28). Note the similarity to Table IV.

	$r_m^{\rm theor}$	$r_m^{\rm expt}$	$\epsilon_m^{\rm theor}$	$\epsilon_m^{\rm expt}$	$R^{\rm CTP}_{\rm theor}$	$R^{\rm CTP}_{\rm expt}$
Xe	4.15	4.15	1.90	2.17	3.18	3.17
Kr	3.75	3.75	2.22	2.13	2.90	2.87
Ar	3.50	3.54	2.51	2.08	2.69	2.72
Ne	2.85	3.21	2.37	2.13	2.14	2.27

$$\sum_f \frac{2}{\epsilon_{fi}^2}\left\langle i\left|\frac{1}{|\vec{r}-\vec{r}'|}\right|f\right\rangle\left\langle f\left|\left[H,\frac{1}{|\vec{r}-\vec{r}'|}\right]\right|i\right\rangle \simeq \frac{2}{\bar{E}^2}\left\langle i\left|\left[\Pi\frac{1}{|\vec{r}-\vec{r}'|}\Pi\right]\left[T,\left[\Pi\frac{1}{|\vec{r}-\vec{r}'|}\Pi\right]\right]\right|i\right\rangle . \quad (53)$$

The trace of the dielectric tensor $\epsilon_{\mu\mu}(\omega,\vec{r},\vec{r}')$ is then given approximately by

$$\frac{1}{3}\sum_\mu \epsilon_{\mu\mu}(0,\vec{r},\vec{r}')\simeq\delta(\vec{r}-\vec{r}')+\frac{\hbar^2e^2}{m\bar{E}^2}\frac{1}{(4\pi)}\nabla^2_{\vec{r}}\nabla^2_{\vec{r}'}\int\frac{1-e^{-\lambda|\vec{r}-\vec{r}'|}}{|\vec{r}-\vec{r}'|}\frac{1-e^{-\lambda|\vec{r}-\vec{r}'|}}{|\vec{r}-\vec{r}'|}\rho(\vec{r})d\vec{r}\,, \quad (54)$$

and may be averaged over a unit cell to obtain the usual expression

$$\epsilon(0)\simeq 1+\left[\frac{\hbar\omega_p}{\bar{E}}\right]^2, \quad (55)$$

where

$$\omega_p=\left[\frac{4\pi e^2}{m}\bar{\rho}\right]^{1/2} \quad (56)$$

is the plasma frequency. The inability of the electrons to respond to low-frequency perturbations over distances shorter than $1/\lambda$ is potentially important in reducing screening at surfaces. van der Waals potentials are known[1] not to be additive, as a result of higher-order diagrams (n-body forces) omitted in Eq. (37). When the probe is far from the surface, these give rise to a van der Waals attraction of the form

$$V(z)=-C_3/(z-z_0)^3 \quad (57)$$

with $z-z_0$ the distance to the surface and C_3 given by[35]

$$C_3=\frac{\hbar}{2\pi}\int_{-\infty}^{\infty}\frac{\epsilon(i\omega)-1}{\epsilon(i\omega)+1}\alpha(i\omega)d\omega\,. \quad (58)$$

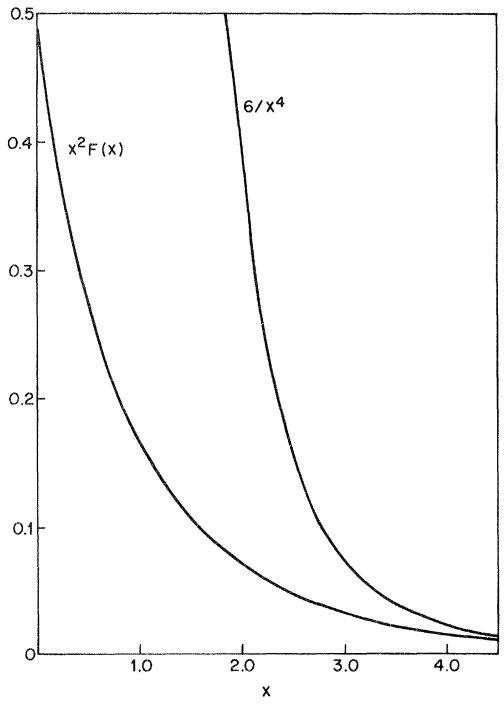

FIG. 14. Comparison of approximate van der Waals kernel $x^2F(x)$ with $6/x^4$. Note that the former is finite at $x=0$.

Screening, which is accomplished by the denominator in Eq. (58), is due physically to the ability of the dielectric to expel low-frequency electric fields. The unscreened version of Eq. (58), obtained by replacing the denominator with 2, gives a value for C_3 for GaAs of ~ 400 meV Å^6, as opposed to the value calculated by Vidali and Cole[36] using Eq. (58) of ~ 160 meV Å^6. However, Eq. (58) is valid only to the extent that the vacuum-solid interface is infinitely sharp. In practice because of momentum dependence of ϵ (Ref. 34) this interface has a width $1/\lambda$ at low frequencies, and thus the fields felt by the surface atoms have values between those immediately inside and outside the surface. Taking as a guess the average, we find that

$$E_z^{\text{atom}} \simeq \frac{E_z^{in}+E_z^{\text{out}}}{2} = \frac{1+\epsilon}{2} E_z^{\text{in}} = E_2^{\text{unscreened}} . \tag{59}$$

Thus, when the probe is very near the surface, the unscreened van der Waals potential, as manifested in Eq. (54), may be more correct that Eq. (59). The success of Tsuchida[15] in predicting the He-LiF potential from a pairwise sum suggests strongly that this is the case.

V. APPROXIMATING THE GaAs(110) POTENTIAL

In principle, the formalism outlined in the preceding section, particularly Eq. (50) and the simpler Eq. (36), should enable one to generate a scattering potential given a charge density for the surface. However, charge densities accurate to 10^{-5} Å^{-3} are rarely calculated and do not presently exist for the relaxed GaAs(110) surface.[37] The best available charge density for this surface, that of Chelikowsky and Cohen[38] is reproduced in Fig. 15. The outermost charge contour, which may be seen to lie roughly 2 Å above the surface As atom, corresponds to a density[38] of 7×10^{-2} Å^{-3}. By exponential extrapolation of this, we conclude that the charge contours most relevant to a 21-meV helium atom lie at the edge of the figure. Since the calculation of charge densities accurate in this region is difficult, we shall concentrate at this stage on determining whether the formalism is approximately correct, and whether the experiment is sufficiently sensitive to nuances in the potential that a simple extrapolation of the pseudopotential results will not do.

We note firstly that Fig. 15 is reminiscent of a

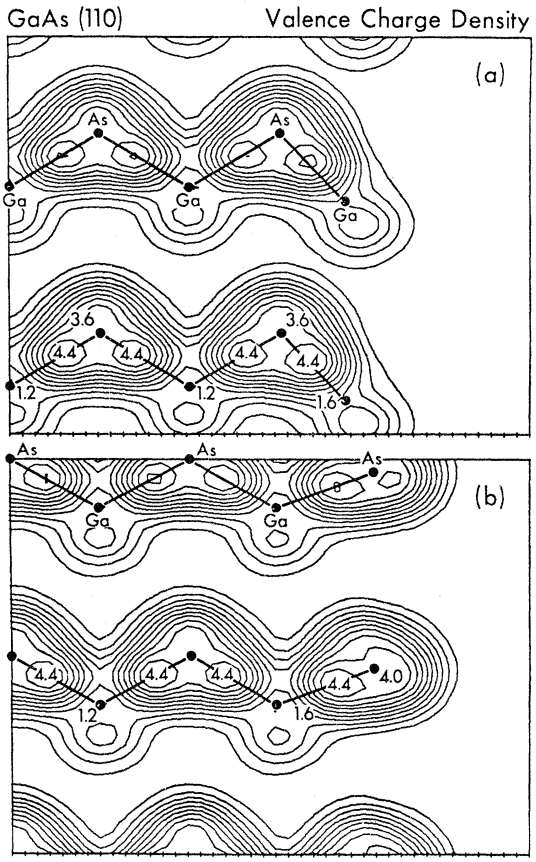

FIG. 15. Total valence pseudo-charge-density for the relaxed GaAs(110) surface as calculated by Chelikowsky and Cohen (Ref. 38). These are cuts through (110) planes other than the (110) plane of the surface. The charge contours are on a linear scale.

superposition of atomic-As charge densities in that (1) most of the charge resides in spherical domains centered on the As nuclei, and (2) the outermost charge contour corresponds to a density roughly twice that of atomic As, as can be seen from Fig. 13. The factor of 2 reflects the double occupancy of the As dangling bond. Secondly, we note that the dangling-bond band lies[38] at the valence-band edge, and thus tails out into the vacuum more slowly than do any other occupied wave functions in the solid. Since the energy of the dangling bond (5.7 eV, the work function of p-type GaAs) is by accident nearly identical to the $4p$ eigenvalue (5.4 eV) of atomic As, the two tail similarly into the vacuum. Therefore a superposition of atomic-As charge densities should be a good approximation to the charge density of the surface in the region of interest. It should be emphasized that this substitution will *not* work for the Ga atoms, because the

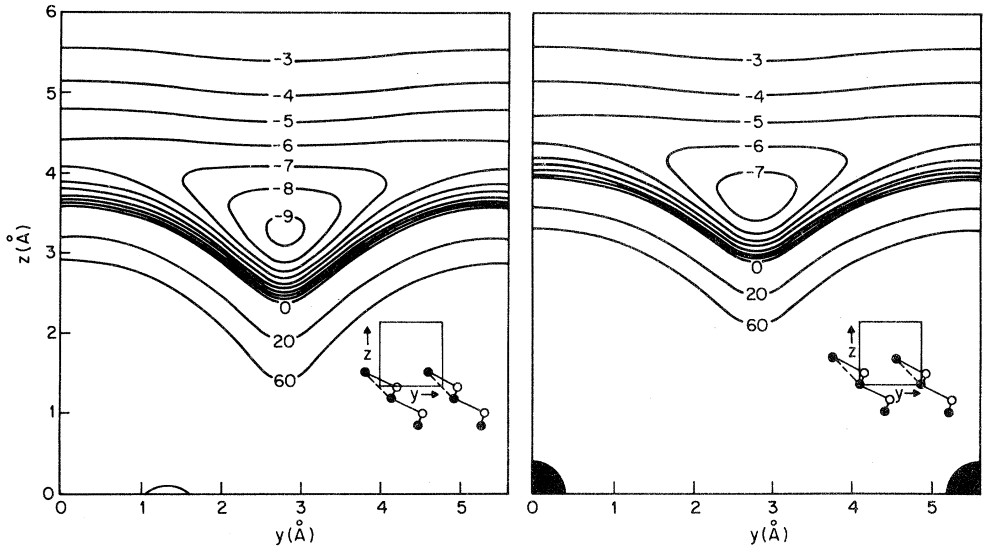

FIG. 16. Potential contours of the model potential constructed from atomic As charge densities. Right-hand side: a plane normal to the surface passing through two As nuclei in *adjacent* chains. Left-hand side: same as right except with the plane displaced along the chains so as to pass through two Ga nuclei. The units of potential are meV.

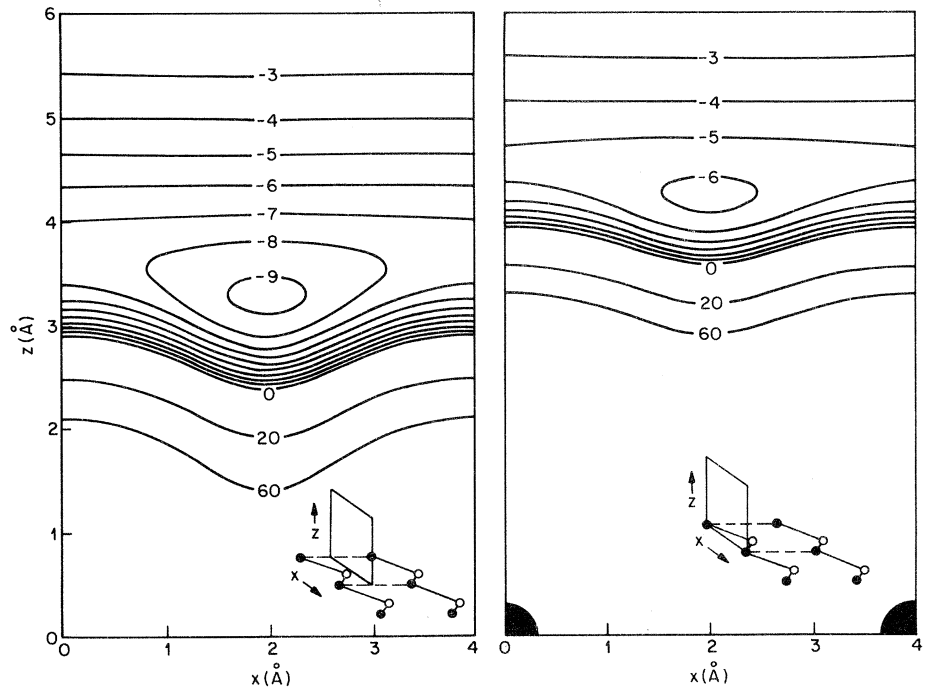

FIG. 17. Potential contours of the model potential constructed from atomic As charge densities. Right-hand side: a plane normal to the surface and passing through two As atoms in the *same* chain. Left-hand side: Same as right, except with the plane displaced across the troughs so as to lie midway between As atoms on adjacent chains. The units of potential are meV.

Ga $4p$ energy is not representative of any energy of the solid. In particular, one can see from Fig. 13 that the Ga $4p$ wave function tails into the vacuum so slowly that atomic Ga actually appears *larger* than atomic As to a 21-meV helium atom, even though As has the same covalent radius and more electrons. An attempt to superimpose atomic Ga and As charge densities to simulate that of the solid would therefore produce the incorrect result that the He atoms were being repelled entirely by the Ga atoms. The case of Ga is a useful counterexample to the notion that the van der Waals potentials of surfaces should be determined simply from properties of the atoms comprising them.

In accordance with these arguments, we take as an approximate GaAs(110) charge density a superposition of atomic As charge densities, multiplied by 2.4 to account for the double occupancy of the dangling bond. Since Eq. (50) is equivalent to the simpler Eq. (36) for atoms, we evaluate the potential using the latter, with C_6 taken to be that calculated from Eq. (40) with $\bar{E}=5.2$ eV taken to be the GaAs Penn gap.[39] For convenience, we place all eight electrons on the As atom to obtain values of $C_6=3.5\times10^4$ meV Å^6 ($N_2=8$) for He-As and $C_6=0$ for He-Ga. The principle effect of associating all the oscillator strength with the As atom is to reduce by $\sim10\%$ the depth of the attractive well above the trough.

In Fig. 16 we show contours of this potential in planes normal to the surface and perpendicular to the troughs. As in Fig. 15, the plane passes through two Ga atoms (left) and two As atoms (right) on adjacent chains. The origin of the horizontal coordinate is the surface plane of the As nuclei *after* reconstruction (the As atom rotates upward by 0.4 Å upon reconstruction.) One can see that the classically forbidden region is very nearly a superposition of spheres of radius 3.5 Å about the As centers, a result consistent with observations made in Sec. IV about additivity of potentials, as well as the 3.5 Å-turning-point radius listed in Table II. The large magnitude of this radius causes the potential to have three qualitative attributes consistent with the data analysis of Sec. III: (1) The peak-to-trough distance of the classical turning-point surface is approximately 1 Å, as opposed to the 2.4 Å one would guess from the vertical separation of the first and second layer As nuclei. (2) The maximum attractive-well depth lies between -5.0 eV and -9.0 eV, values bounding the 7 meV guessed from the calculation of Fig. 9. (3) The corrugation along the trough is roughly 0.3 Å. This latter effect can be seen more clearly in Fig. 17, in which the observation plane has been rotated 90° in the surface so as to bisect a trough (left) or a ridge (right). The corrugation of the trough is slightly larger than 0.3 Å due to the failure of the As core to effectively fill in the bottom. The ridge corrugation is the 0.2 Å indicated by the experiment.

With the qualitative aspects of the potential accounted for, we turn to the question of how well these crude approximations can account for the scattering signal. In the left column of Fig. 18 we show 21-meV across-trough diffraction patterns for the potential of Figs. 16 and 17. The agreement with experiment is clearly not good. However, we note that the rainbow is properly collapsed at $\theta_i=61°$, in agreement with Fig. 6, and that at $\theta_i=45°$, a very small rainbow can be seen four beams to the left of specular, at $\theta_R=0°$. This is consistent in location with that of Fig. 3 (five

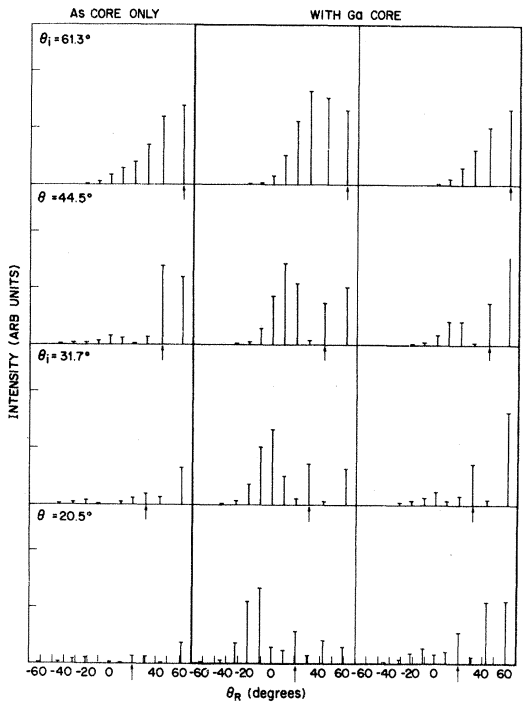

FIG. 18. Across-trough diffraction patterns calculated for the model potential discussed in the text without (left-hand column) and with (right-hand column) a Ga core. The incident energy is 21 meV. Intensity is plotted vs θ_R, the polar angle of exit of the probe, for various values of θ_i, the polar angle of incidence. The middle and right columns correspond to particles being incident on the side of the ridge with and without the Ga atom, respectively. Note that the presence of the Ga core restores power to the primary rainbow.

beams away, rather than four) but obviously not in magnitude. At $\theta_i = 32°$, this small rainbow has moved to $\theta_R = -20°$, and a new rainbow appears to be emerging from the specular beam. There is no evidence of this new rainbow at $\theta_i = 21°$, however. We interpret these results as implying that the rainbow pattern characteristic of the corrugation is, in fact, reproduced by this potential, but that the scattering power into the rainbows is insufficient.

In light of the semiclassical interpretation of beams powers as manifestions of the radius of curvature of the surface at the classical impact point, lack of intensity can easily be attributed to the presence of cusps in the sides of the ridges where the As cores come together. These may be seen in the left half of Fig. 19, in which potential contours in a plan parallel to the surface and 3.5 Å above the As nuclei are plotted. The repulsive cores, located at the corners may be seen to form wasp-waisted ridges which have no characteristic slope across the trough except at symmetry points. This potential therefore scatters extensively out of plane at the expense of rainbow intensity. The inadequacy of this potential is most likely due to an unforeseen tendency of the real charge density to smooth and mend itself at these distances. One mechanism by which might be accomplished is the forced orthogonolization of the As dangling-bond states to the Ga states involved in bonding. This would tend to make the charge avoid the Ga atoms and bulge out slightly above the Ga sites, thus tending to smooth the cusp on one side of the ridge.

To investigate this possibility, we have performed scattering calculations on the potential of Figs. 16 and 12 modified to include a Ga core. Since use of the atomic Ga charge density would not be physically sensible, we have taken the Ga charge density to be that of As, multiplied by a factor $\gamma = 0.68$, picked to give optimal agreement with experiment. The results of the scattering calculations performed on this potential are shown in the right two columns of Fig. 18. As in Fig. 6 the two columns correspond to particles impinging on the shallow (middle) and steep (right) sides of the ridge. Both sides shown resurrected rainbow power and a slightly reduced (three beams from specular, as opposed to four) rainbow angle. The shallow side, which is made so by the presence of the Ga core's puffing out the side of the trough,

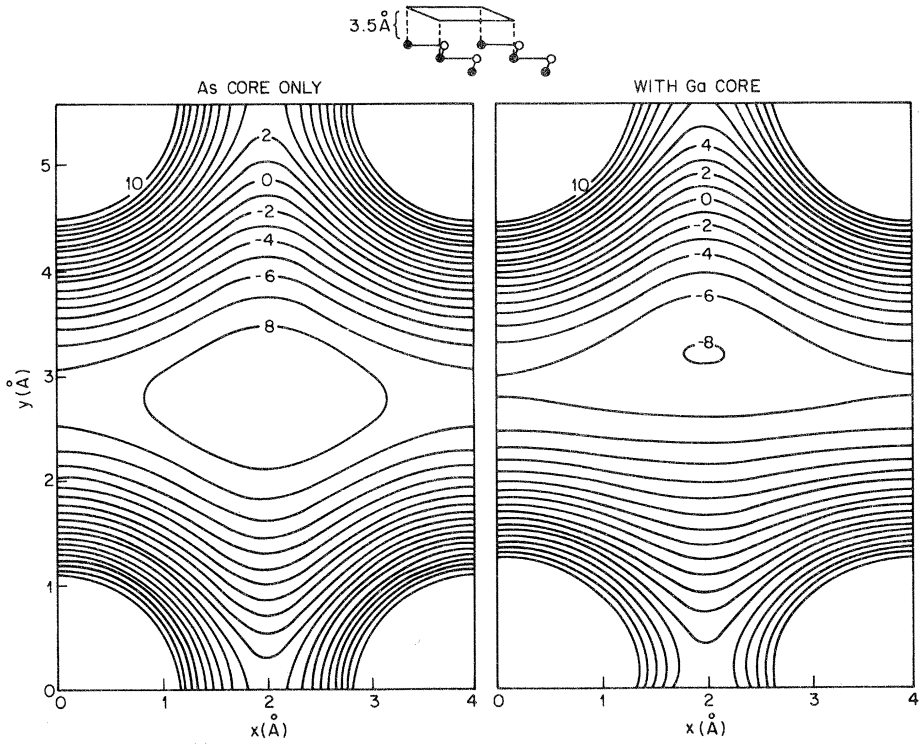

FIG. 19. Potential contours of the model potential constructed from atomic As charge densities without (left) and with (right) a Ga core. This is a plane parallel to the surface 3.5 Å above the As nuclei. The As repulsive core can be seen encroaching at the corners. Note the cusp in the side of the ridge where the As cores come together. The units of potential are meV.

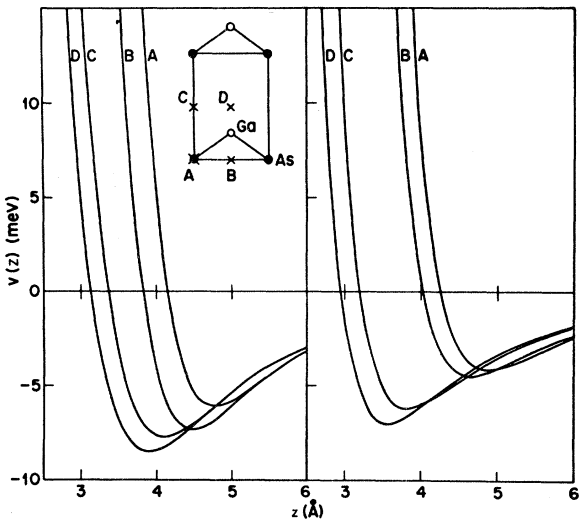

FIG. 20. Comparison of empirical potential (left) described Eq. (15) and producing Fig. 9(d) with the model potential (right) constructed from atomic As charge densities with no Ga core. These are plots of potential vs height above the surface at symmetry points in the surface unit cell. The origin of z for the model potential is the center of the As atom before reconstruction (it moves upward 0.4 Å upon reconstruction). The origin of z for the empirical potential has been adjusted to obtain agreement with the model potential.

shows a fully developed rainbow at $\theta_i = 45°$, 32°, and 21°, and complete collapse of this rainbow by $\theta_i = 61°$. The steep side shows similar behavior, except that the degree of resurrection is smaller. We note that an attempt to make the core larger restores more power to the steep rainbow while simultaneously reducing the rainbow angle for both sides. Making it smaller robs power from the steep rainbow. It therefore seems clear that while the addition of a Ga core is helpful in explaining smoothing in qualitative terms, it is not a good procedure for producing potentials which can scatter in quantitative agreement with experiment. A contour plot of the potential generating these columns of Fig. 18 is shown on the right of Fig. 19.

While it is possible that a simple way to generate surface charge densities to sufficient accuracy may yet be discovered, it seems more likely that the evident sensitivity of the scattering signal to nuances in the potential will require that a thorough surface charge-density calculation, capable of taking band-structure effects in the solid, and possibly self-consistency, into account, be performed before one can calculate diffraction intensities reliably.

To illustrate the sensitivity to aspects of the potential of little interest in structural analysis, we compare in Fig. 20 the potential generating Figs. 16 and 17 (which does not give good intensities) with the empirical potential generating Fig. 9(d) (which does). The four curves in each case are potential as a function of distance above the surface at symmetry points in the surface unit cell. The curves on the right are a reproduction of Figs. 16 and 17 with the origin of z now the center of the As atom in the unrelaxed position. The curves on the left are those generated by Eq. (15), up to an arbitrary adjustment of the origin of z to bring the two sides of the figure into registry. These sets of curves are identical in the sense that they reflect a peak-to-trough distance of roughly 1 Å, a corrugation along the troughs of $\frac{1}{5}$ of this, and an attractive-well depth of approximately 7 meV. Nevertheless they scatter very differently. From comparisons of this kind we come to the unpleasant conclusion that subtle errors in a potential can completely destroy its ability to scatter in agreement with experiment.

VI. SUMMARY

In this paper we have attempted to shed some light on the generation of helium-surface potentials by investigating, in detail, diffraction from a highly corrugated surface with a known structure.[5] We have shown that GaAs(110) scatters quantitatively as though it were a soft wall sinusoidally corrugated across the trough with an effective peak-to-trough distance of 1.1 Å. We have performed close-coupling scattering calculations on a sequence of model potentials with successively deeper attractive wells and have found trends in the results which suggest that the depth is 7 meV. We have reviewed the problem of first-principles generation of scattering potentials and have suggested that existing methods[14] will not work for helium, as opposed to larger closed-atoms, because of its small size. We have proposed new procedures for generating these potentials consistent with the recent work of Esjberg and Nørskov,[16] and have shown these to work effectively for rare-gas targets. We have then applied these rules to GaAs(110) and have shown them to be consistent with our empirical fits, up to inaccuracies in the GaAs(110) charge density. These rules show the classical turning point surface lying 3.5 Å above the As nucleus.

ACKNOWLEDGMENTS

I would like to thank M. Cardillo and D. Miller for helpful concerning the GaAs(110) data. D. Hamann was instrumental in providing the local-density atomic charge densities and in discussing theoretical aspects of the problem. I would also like to thank M. W. Cole, J. C. Phillips, G. Vidali, D. R. Frankl, N. Garcia, V. Celli, N. Lang, and C. B. Duke for helpful criticism.

APPENDIX: COMPUTATIONAL TECHNIQUE

The method outlined below for solving the single-particle Schrödinger equation in the presence of a potential $V(x,y,z)$ periodic in x and y and infinitely repulsive as $z\rightarrow-\infty$ is a Green's-function technique similar to that used by Mele and Joannopoulos[40] for calculating surface electronic structures in a tight-binding basis. The primary advantage over shooting[11,41] methods is that the system satisfied Dirichlet boundary conditions at every stage of the integration so that inaccuracies resulting from exponential divergences do not occur. Another advantage is that a simple sum rule forces the scattering to be unitary so long as the potential is real.

Following Wolken,[9] we first exploit surface periodicity by transforming to the Laue representation.[41] Letting $\vec{r}$ denote the position coordinate in the plane of the surface and z the normal coordinate, we write the wave function in the form

$$\psi(x,y,z)=\sum_{\vec{G}} A_G(z)e^{i(\vec{k}+\vec{G})\cdot\vec{r}}\ , \tag{A1}$$

where $\vec{k}$ is the crystal momentum in the plane of the surface and $\vec{G}$ is a surface reciprocal-lattice vector. We collect the coefficients $A_{\vec{G}}$ into a vector $|A(z)\rangle$, the components of which are given by

$$\langle\vec{G}\,|\,A(z)\rangle=A_{\vec{G}}(z)\ , \tag{A2}$$

and write the wave equation in the form

$$-\frac{\hbar^2}{2m}\frac{\partial^2}{\partial z^2}\,|\,A(z)\rangle=[E-T-V(z)]\,|\,A(z)\rangle\ , \tag{A3}$$

where

$$\langle\vec{G}\,|\,T\,|\,\vec{G}'\rangle=\frac{\hbar^2}{2m}\,|\,\vec{k}+\vec{G}\,|^2\delta_{\vec{G}\,\vec{G}'}\ , \tag{A4}$$

and

$$\langle\vec{G}\,|\,V(z)\,|\,\vec{G}'\rangle=\frac{1}{\Omega}\int V(\vec{r},z)e^{-i(\vec{G}-\vec{G}')\cdot\vec{r}}d\vec{r} \tag{A5}$$

are matrices and E is the energy. Ω is the area of the surface unit cell. This is then converted to a difference equation in z in the manner

$$-\frac{\hbar^2}{2m}\frac{|A_{n+1}\rangle+|A_{n-1}\rangle-2\,|A_n\rangle}{(\Delta z)^2}=(E-T-V_n)\,|A_n\rangle\ , \tag{A6}$$

where $z=n\Delta z$, and rewritten in the form

$$(E-E_n)\,|A_n\rangle=D(\,|A_{n-1}\rangle+|A_{n+1}\rangle)\ , \tag{A7}$$

where

$$\langle\vec{G}\,|\,D\,|\,\vec{G}'\rangle=-\frac{\hbar^2}{2m\,(\Delta z)^2}\delta_{\vec{G}\,\vec{G}'}\ , \tag{A8}$$

and

$$E_n=T+V_n-2D\ . \tag{A9}$$

The matrices D and E_n are then truncated to a large but finite number of reciprocal-lattice vectors. In the case of the two-dimensional calculations of Figs. 9 and 10, convergence was obtained with an 11×19 rectangular grid of $\vec{G}'$, or 209 degrees of freedom, when $\vec{k}$ does not lie along a symmetry direction. The step size was typically $\Delta z=0.1$ Å for the 21-meV calculations. In no case was a size $\Delta z=0.05$ Å a significant improvement.

Our method of solving Eq. (A7) is the Koster-Slater technique applied to a one-dimensional chain with nearest-neighbor interactions. This technique is based on the observation that if a perturbation V commutes with a projection operator $\Pi=\Pi^2$ in the manner

$$\Pi V\Pi=V\ , \tag{A10}$$

then the Green's function G of the system in the presence of V, written in terms of G_0, the Green's function in the absence of V, in the manner

$$G=G_0\sum_n(VG_0)^2\ , \tag{A11}$$

satisfies the equation

$$\Pi G\Pi=(\Pi G_0\Pi)\sum_n(V\Pi G_0\Pi)^2\ . \tag{A12}$$

In the present case, the perturbation V is the hopping interaction D between the nth and $(n+1)$st links and Π is the projector of these two links.

We consider firstly the situation in which all

hopping interactions for links $m<n$ are turned on while all those for $m>n+1$ are turned off. We have a chain of length n which we will make into a chain of length $n+1$ by turning on D. Letting F_n denote the Green's function of the chain of length n confined to the nth link, we have by Eq. (A12)

$$\Pi G \Pi = \begin{bmatrix} F_n^{-1} & D \\ D & E-E_{n+1} \end{bmatrix}^{-1} . \tag{A13}$$

This can be evaluated in closed form in terms of F_n as

$$\Pi G \Pi = \begin{bmatrix} f_n + F_n D X D F_n & F_n D X \\ X D F_n & X \end{bmatrix} , \tag{A14}$$

where

$$X = (E - E_{n+1} - D F_n D)^{-1} . \tag{A15}$$

Since this process simply lengthens the chain, we have

$$F_{n+1} = (E - E_{n+1} - D F_n D)^{-1} . \tag{A16}$$

Equation (A16) enables one to calculate F_n for some n outside the surface, where the potential V_n has gone to zero, by a sequence of matrix inversions, starting from a known value of F_0 deep inside the classical turning-point surface. This value is essentially zero, since E_0 in this region is dominated by the large positive diagonal-matrix elements of V_0. The assumption of $F_0=0$ is physically equivalent to the assumption that probe particles do not penetrate to $z=0$. The iterative procedure can also be performed for the vacuum, the case in which $V_n=0$ for all n, provided the vacuum self-energy E_{vac}, given by

$$E_{\text{vac}} = T - 2D \tag{A17}$$

is given a small absorptive component in the manner

$$E_{\text{vac}} \rightarrow E_{\text{vac}} - i\delta . \tag{A18}$$

The iterative equations, given by

$$F_{\text{vac}} = (E - E_{\text{vac}} - D F_{\text{vac}} D)^{-1} , \tag{A19}$$

may also be solved analytically in the manner

$$F_{\text{vac}} = \frac{(E - E_{\text{vac}}) \pm [(E - E_{\text{vac}})^2 - 4D^2]^{1/2}}{2D^2} , \tag{A20}$$

where, in the $\vec{G}$ representation (in which E_{vac} and D are diagonal) the boundary condition equation (A18) is met by selecting the sign of the square root for each term which minimizes the magnitude of the term when real and which makes it absorptive (negative imaginary part) when complex.

We consider secondly the situation in which all the hopping interactions except that between the nth and $(n+1)$st link are turned on. The chain of length n is now converted to the complete-scattering problem by turning on D. Letting G denote the Green's function of the complete system confined to the $(n+1)$st link, we have from Eqs. (A12) and (A19)

$$G = (E - E_{n+1} - D F_n D - D F_{\text{vac}} D)^{-1} . \tag{A21}$$

Similarly, for the vacuum we have

$$\begin{aligned} G_{\text{vac}} &= (E - E_{\text{vac}} - 2D F_{\text{vac}} D)^{-1} \\ &= 1/[(E - E_{\text{vac}})^2 - 4D]^{1/2} . \end{aligned} \tag{A22}$$

G carries information both about the scattering and about the reactive response of the medium in the absence of the surface. As the latter is also carried by G_{vac}, we have that $(G - G_{\text{vac}})|\vec{G}\rangle$ describes the *reflected* wave at $n+1$ resulting from the application at $n+1$ of a point source having periodicity $\vec{k}+\vec{G}$ in the plane of the surface. The current carried outward by this wave must be calculated using the discreet momentum operator, which in one dimension takes the form

$$p\,|n\rangle = \frac{\hbar}{i\Delta z}(|n+1\rangle - |n\rangle) . \tag{A23}$$

Since the analog of Eq. (A14) in this case is

$$\begin{bmatrix} G & G D F_{\text{vac}} \\ F_{\text{vac}} D G & F_{\text{vac}} + F_{\text{vac}} D G D F_{\text{vac}} \end{bmatrix} , \tag{A24}$$

the current density in the $\vec{G}$th channel is given by

$$\begin{aligned} J_{\vec{G}} = &-\frac{\hbar}{m\Delta z} \mathrm{Im}\langle \vec{G}' | D F_{\text{vac}} | \vec{G}' \rangle \\ &\times |\langle \vec{G}' | G - G_{\text{vac}} | \vec{G} \rangle|^2 . \end{aligned} \tag{A25}$$

The total current density absorbed by the system is given by

$$J = \frac{2\Delta z}{\hbar} \mathrm{Im}\langle \vec{G} | G_{\text{vac}} | \vec{G} \rangle . \tag{A26}$$

Since G_{vac} is related to F_{vac} by

$$-2\,\mathrm{Im}\langle \vec{G} | D F_{\text{vac}} D | \vec{G} \rangle = 1/\mathrm{Im}\langle \vec{G} | G_{\text{vac}} | \vec{G} \rangle , \tag{A27}$$

the scattering probabilities $I_{\vec{G}\,\vec{G}'}$ are given by

$$I_{\vec{G}\,\vec{G}'}=\frac{|\langle\vec{G}'|G-G_{\rm vac}|\vec{G}\rangle|^2}{{\rm Im}\langle\vec{G}'|G_{\rm vac}|\vec{G}'\rangle{\rm Im}\langle\vec{G}|G_{\rm vac}|\vec{G}\rangle}\ . \tag{A28}$$

Unitary of Eq. (A28) may be verified by noting that

$$\langle\vec{G}'|G-G_{\rm vac}|\vec{G}\rangle=\langle\vec{G}'|G|\vec{G}\rangle-\langle\vec{G}'|G_{\rm vac}\vec{G}'\rangle\delta_{\vec{G}\,\vec{G}'}\ . \tag{A29}$$

Since

$$\frac{\hbar}{m\Delta z}\sum_{\vec{G}'}{\rm Im}\langle\vec{G}'|DF_{\rm vac}|\vec{G}'\rangle|\langle\vec{G}'|G|\vec{G}\rangle|^2=\frac{2\Delta z}{\hbar}{\rm Im}\langle\vec{G}|G|\vec{G}\rangle\ , \tag{A30}$$

and

$$\langle\vec{G}|G_{\rm vac}\vec{G}\rangle=-\langle\vec{G}|G_{\rm vac}|\vec{G}\rangle\ , \tag{A31}$$

so that

$$|\langle\vec{G}|G-G_{\rm vac}|\vec{G}\rangle|^2-|\langle\vec{G}|G|\vec{G}\rangle|^2=|\langle\vec{G}|G_{\rm vac}|\vec{G}\rangle|^2-2\,{\rm Im}\langle\vec{G}|G_{\rm vac}|\vec{G}\rangle{\rm Im}\langle\vec{G}|G|\vec{G}\rangle\ , \tag{A32}$$

one has

$$\frac{\hbar}{m\Delta z}\sum_{\vec{G}'}{\rm Im}\langle\vec{G}'|DF_{\rm vac}|\vec{G}'\rangle|\langle\vec{G}'|G-G_{\rm vac}|\vec{G}\rangle|^2$$
$$=\frac{\hbar}{m\Delta z}{\rm Im}\langle\vec{G}|DF_{\rm vac}|\vec{G}\rangle|\langle\vec{G}|G_{\rm vac}|\vec{G}\rangle|^2=\frac{2\Delta z}{\hbar}{\rm Im}\langle\vec{G}|G_{\rm vac}|\vec{G}\rangle\ . \tag{A33}$$

[1] An excellent review of the field of atom-surface interactions may be found in H. Hoinkes, Rev. Mod. Phys. 52, 933 (1980).

[2] M. W. Cole and D. R. Frankl, Surf. Sci. 70, 585 (1978).

[3] K. H. Rieder, T. Engel, and N. Garcia, Proc. I.V.C. and ECOSS IV (LeVide, LeCouche Minces, Suppl. 201, 1980), p. 861.

[4] M. J. Cardillo and G. E. Becker, Phys. Rev. Lett. 40, 1148 (1978); 42, 508 (1979); Phys. Rev. B 4, 1497 (1980).

[5] M. J. Cardillo, G. E. Becker, S. Sibener, and D. R. Miller, Surf. Sci. 107, 469 (1981).

[6] G. Derry, D. Wesner, W. E. Carlos, and D. R. Frankl, Surf. Sci. 87, 629 (1979); G. Boato, P. Cantini, C. Guidi, R. Tatarek, and G. P. Felcher, Phys. Rev. B 20, 3957 (1980); N. Garcia, W. E. Carlos, M. W. Cole, and V. Celli, *ibid.* 21, 1638 (1980); W. E. Carlos and M. W. Cole, *ibid.* 21, 3713 (1980).

[7] G. Boato, P. Cantini, and L. Mattera, Surf. Sci. 55, 141 (1976).

[8] N. Garcia, J. Chem. Phys. 67, 897 (1977).

[9] G. Wolken, J. Chem. Phys. 58, 3047 (1973).

[10] C. E. Harvie and J. H. Weare, Phys. Rev. Lett. 40, 187 (1978).

[11] W. E. Carlos, G. Derry, and D. R. Frankl, Phys. Rev. B 19, 3258 (1979).

[12] W. E. Carlos and M. W. Cole, Phys. Rev. Lett. 43, 697 (1979).

[13] D. L. Freeman, J. Chem. Phys. 62, 941 (1975).

[14] R. G. Gordon and Y. S. Kim, J. Chem. Phys. 56, 3122 (1972).

[15] A. Tsuchida, Surf. Sci. 46, 611 (1971).

[16] N. Esjberg and J. Nørskov, Phys. Rev. Lett. 45, 807 (1980); see also E. Zaremba and W. Kohn, Phys. Rev. B 15, 1769 (1977).

[17] D. J. Chadi, Phys. Rev. B 19, 2074 (1979), and references therein.

[18] U. Garibaldi, A. C. Levi, R. Spasacini, and G. E. Tommei, Surf. Sci. 48, 649 (1975).

[19] N. Garcia, V. Celli, and F. O. Goodman, Phys. Rev. B 19, 634 (1979).

[20] J. W. Strutt (Baron Rayleigh), *The Theory of Sound* (Macmillan, London, 1896), Vol. II, p. 272.

[21] G. R. Armand and J. R. Manson, Phys. Rev. Lett. 43, 1839 (1979).

[22] E. Clementi, IBM J. Res. Dev. Suppl. 9, 2 (1965).

[23] P. Bertoncini and A. C. Wahl, Phys. Rev. Lett. 25, 991 (1970).

[24] W. A. Steele, Surf. Sci. 36, 317 (1973).

[25] N. D. Lang, Phys. Rev. Lett. 46, 842 (1981).

[26] F. Herman and S. Skillman, *Atomic Structure Tables* (Prentice-Hall, Englewood Cliffs, 1963).

[27] E. P. Wigner, Phys. Rev. 46, 1002 (1934).

[28] C. H. Chen, P. E. Siska, and Y. T. Lee, J. Chem. Phys. 59, 601 (1973).

[29] A. Dalgarno, Adv. Chem. Phys. 12, 143 (1967); G. Starkschall and R. G. Cordon, J. Chem. Phys. 54,

663 (1971).
[30]K. T. Tang, J. M. Norbeck, and P. R. Certain, J. Chem. Phys. 64, 3063 (1976).
[31]R. A. Aziz, P. W. Riley, U. Buck, G. Maneke, J. Schleusener, G. Scoles, and U. Valbusa, J. Chem. Phys. 71, 2637 (1979).
[32]M. Keil, J. T. Slankas, and A. Kuppermann, J. Chem. Phys. 70, 482 (1979).
[33]P. W. Langhoff, R. G. Gordon, and M. Karplus, J. Chem. Phys. 55, 2126 (1971).
[34]J. Bernholc and S. T. Pantelides, Phys. Rev. B 15, 4935 (1977), and references therein.
[35]See, for example, R. G. Barrera, and C. B. Duke, Phys. Rev. B 14, 3695 (1976).
[36]G. Vidali and M. W. Cole, Surf. Sci. 107, L-374 (1981).
[37]Since completion of this manuscript, calculations of the GaAs(110) charge density in the region relevant to helium scattering have been reported by D. R. Hamann, Phys. Rev. Lett. 46, 1227 (1981). These calculations are consistent with the present analysis, including the tendency to scatter with indistinct rainbows.
[39]J. C. Phillips, *Bonds and Bonds in Semiconductors* (Academic, New York, 1973), p. 12.
[40]E. J. Mele and J. D. Joannopoulos, Phys. Rev. B 17, 1816 (1978).
[41]J. A. Appelbaum and D. R. Hamann, Rev. Mod. Phys. 48, 479 (1976).